Spreading and Vertical Structure of the Persian Gulf and Red Sea Outflows in the Northwestern Indian Ocean

Pierre L'Hégaret, Charly De Marez, Mathieu Morvan, Thomas Meunier, Xavier Carton

JGR Oceans

RESEARCH ARTICLE
10.1029/2019JC015983

Key Points:

- A detection method and metrics are developed here to capture salty water mass cores and quantify their salinity gradients and interleaving
- Persian Gulf and Red Sea Waters diminishes in salinity with distance from their straits of exit, undergoing important layering
- Stronger loss in salinity are observed in the regions filled with mesoscale eddies

Correspondence to:
P. L'Hégaret,
pierre.lhegaret@outlook.fr

Citation:
L'Hégaret, P., de Marez, C., Morvan, M., Meunier, T., & Carton, X. (2021). Spreading and vertical structure of the Persian Gulf and Red Sea outflows in the northwestern Indian Ocean. *Journal of Geophysical Research: Oceans*, *126*, e2019JC015983. https://doi.org/10.1029/2019JC015983

Received 20 DEC 2019
Accepted 21 MAR 2021

Spreading and Vertical Structure of the Persian Gulf and Red Sea Outflows in the Northwestern Indian Ocean

Pierre L'Hégaret[1,3], Charly de Marez[1], Mathieu Morvan[1,4], Thomas Meunier[2,5], and Xavier Carton[1]

[1]Laboratoire d'Océanographie Physique et Spatiale (LOPS), IUEM, Technopôle Brest-Iroise, Plouzané, France, [2]Ensenada Center for Scientific Research and Higher Education, CICESE, Ensenada, Mexico, [3]Now at Laboratoire de Météorologie Dynamique, IPSL, Ecole Normale Supérieure, Paris, France, [4]Now at SHOM, Service Hydrographique et Océanographique de la Marine, Brest CEDEX 2, France, [5]Now at Woods Hole Oceanographic Institution, Falmouth, Massachusetts, USA

Abstract In the Indian Ocean, salty water masses from the Persian Gulf and Red Sea are important sources of salt, heat, and nutrients. Across the Arabian Sea, these outflows impact human and biological activities, their thermohaline characteristics and shapes exhibiting important spatial and seasonal variability. The knowledge of the water masses properties is important to validate realistic simulations of the Indian Ocean. A classical approach to study these water masses is to track them on specific isopycnal levels. Nevertheless, their peaking thermohaline characteristics are not always found at a specific density but rather spread over a range. Here, we develop a detection algorithm able to capture the full vertical structure of the outflows, that we applied to a data set of about 126,000 vertical profiles. We are thus able to quantify the changes in their thermohaline signatures and in their vertical structures, characterized here by the intensity of the salinity peaks of the water masses and lateral injection of fresh and salty waters, and describe their spatial variability. Across the northwestern Indian Ocean, the salty outflows undergo several changes, diminishing their thermohaline signatures and peaks and layering. In their early stages in the narrow Gulf of Oman and Aden, the outflows present configurations indicative of diapycnal mixing. In the same regions and along the western edge of the Arabian Sea, these water masses are subject to lateral mixing. All over the Arabian Sea, salt fingering conditions are met for lower layers of the outflows.

Plain Language Summary In the northwestern Indian Ocean, water masses with different characteristics are measured. Two of them are some of the most salty found globally, namely Persian Gulf Water and Red Sea Water. In the Arabian Sea, these outflows transport salt and heat, affecting the biological activity. Furthermore, the knowledge of such quantities is necessary to simulate the circulation of the basin. A classical approach to analyze the characteristics of these outflows is to measure them at specific densities. It has been observed that peaks in salinity are more often found over a range of densities, rather than at specific values. In this study, we develop a detection algorithm able to capture the full vertical structure of the outflows. Thus, we quantify the temperature and salinity regional distribution of the outflows, and describe their vertical configurations. Along their paths, the salty outflows undergo several changes in their vertical structures, with a diminution of their peaks in salinity and lateral injections of saltier and fresher waters, particularly near their straits of exit. Finally, all over the Arabian Sea, the outflows are in salt fingering conditions, losing salt at smaller vertical scales.

1. Introduction

The northwestern Indian Ocean, encompassing the Arabian Sea, is a region where water masses with various characteristics interact with each other. Two of them, exhibiting high salinity values, originate from semi-closed basins subject to important evaporation: the Red Sea and Persian Gulf (Cember, 1988; Yao & Johns, 2010). As these outflows spread out of their basins of formation, in the Gulf of Aden and Oman (see Figure 1 for locations), they plunge and are diluted, losing salt and heat, and equilibrate (Prasad et al., 2001; Shapiro & Meschanov, 1991). Nevertheless, traces of the Red Sea Water (RSW) and Persian Gulf Water (PGW) are still found in the Indian Ocean, leaking toward the Atlantic Ocean (Durgadoo et al., 2017) and even more substantially to the neighboring Bay of Bengal (Sheehan et al., 2020). Across the Arabian Sea,

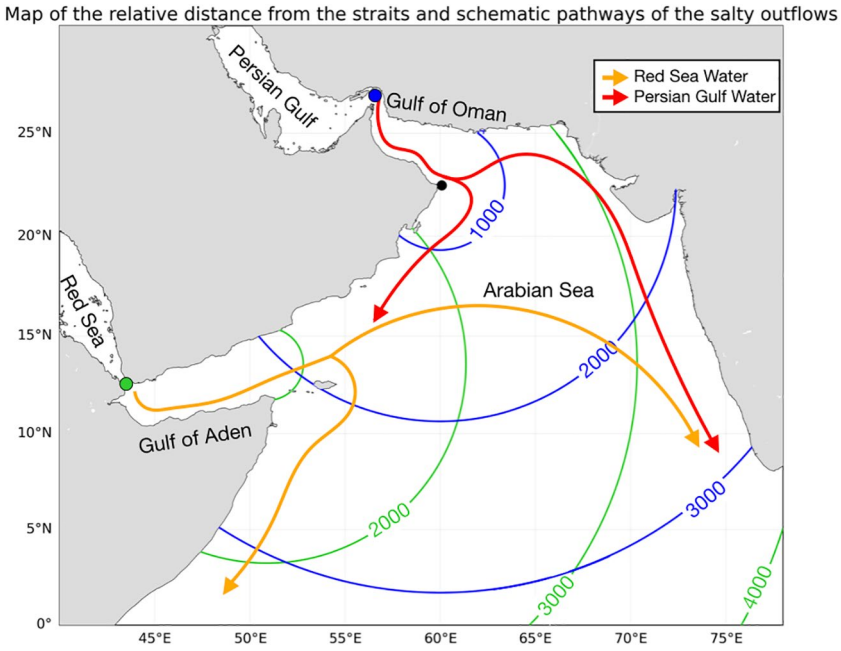

Figure 1. Map of the Arabian Sea and adjacent basins encompassed in the northwestern Indian Ocean. RS and PG correspond to the Red Sea and Persian Gulf, respectively. Relative distances from the straits of exit are shown. Green: out of the Red Sea, the distance is calculated from Bab-el-Mandeb indicated by the green dot. Blue: out of the Persian Gulf, the distance is calculated from the Strait of Hormuz (blue dot). The black dot shows the position of Ra's al-Hadd. The orange and red arrows are the schematic pathways of the Red Sea Water and Persian Gulf Water, respectively.

these outflows display complex biogeochemical responses. Mesoscale eddies advecting PGW transport oxygen into oxygen minimum zones (Queste et al., 2018). Oppositely, its nutrient transport has almost no impact on the intermediate water nutrient concentrations (Morrison et al., 1998).

In recent years, realistic simulations of the Arabian Sea expanded our understanding of the dynamics of the basin and of the water masses spread (Chang et al., 2008; L'Hégaret et al., 2015; Pous et al., 2015; Yao & Johns, 2010). The basin-scale circulation is mainly driven by the monsoon regime, leading to a strong seasonal variability in the shape of mesoscale eddies. These structures influence the paths of the salty outflow. In the Arabian Sea, the RSW mainly spreads northeast along the coast of Yemen and Oman at the periphery of mesoscale eddies and southward along the coast of Somali, with a strong seasonal influence of the Great Whirl (J. Fischer et al., 1996; Schott & Fischer, 2000). The PGW is present throughout the Gulf of Oman, distributed by eddies (Vic et al., 2015), until the outflow reaches Ra's al Hadd, then mostly following a southeastern path (Prasad et al., 2001). Nevertheless, realistic models had trouble simulating the outflows either at correct depth or isopycnal levels. Observations are necessary to correctly configure them or relax their results to the observations (Ilıcak et al., 2011). To improve our understanding of these outflows, we propose here to map and describe the evolution of their thermohaline characteristics, vertical shapes, and variability, from their entrance into the northwestern Indian Ocean to their equilibrium. A second objective here is to assess the main advecting and mixing mechanisms affecting these outflows.

Over the last decade, the number of measurements in the Arabian Sea has drastically increased, thanks to Argo floats (see Figure 2). Analyses of these in situ observations have permitted a description of the thermocline variations (Li & Wang, 2015). Below the thermocline, using all historical and recently available measurements of temperature, salinity, and pressure in the Arabian Sea, we develop an algorithm that allows us to detect the presence of the salty outflows. Defining the vertical boundaries of the water masses is a subjective choice. There, we set them as the spiciness lows found below and above a peak, in an a priori chosen density and depth ranges from observational studies (L'Hégaret et al., 2015; Prasad et al., 2001; Shetye et al., 1994). These horizontal and vertical coordinates allow us to describe the outflows' characteristics in different aspects.

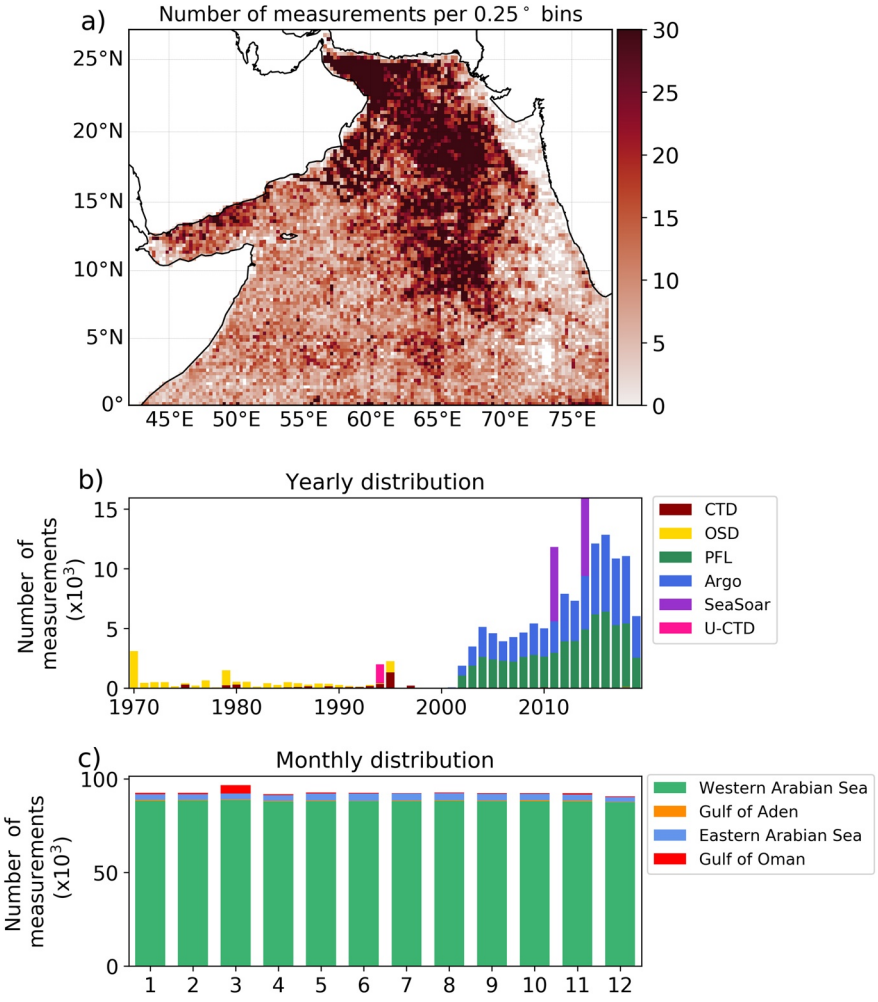

Figure 2. Spatial and temporal distributions of the data. (a) Number of profiles per 0.25° × 0.25° box. (b) Yearly distribution of the profiles with the instrument type color-coded, CTD stands for Conductivity-Temperature-Depth instruments, OSD means Ocean Station Data, and PFL is short for Profiling Floats; bar before 1970 summed all historical measurements done since the 1850s. (c) Monthly distribution with each basin color-coded, which corresponds to the areas defined in Figure 3.

With distance from their straits, the water masses undergo changes in temperature, salinity, and potential density. At first, they undergo quick and important losses when cascading down the continental slope. Across the gulfs and in the western Arabian Sea, the water masses are quickly torn apart via the mesoscale eddies, injecting fresher water at their rims, but also forming submesoscale turbulence and internal waves when interacting with the topographic slope (de Marez et al., 2019, 2020; Morvan et al., 2020). The impact of these turbulent mechanisms is pointed out by a metric we develop here to quantify the interleaving. Then, further offshore, they reach an equilibrium in potential density. We also notice that isolated and highly saline profiles, detected here via a metric averaging the salinity gradients over the outflow core, are rarely captured far from the gulfs. Finally, we observe that all over the Arabian Sea, these outflows advecting warm and salty waters in the Indian Ocean are in favorable conditions for salt fingering at the deeper boundary of the cores.

This study is presented as follows:

– We introduce the different data sets used for our analysis in the data and methods section hereafter. The detection algorithm is detailed, and the water masses are quantified using three different diagnostics

- First, the thermohaline recordings, displayed as a function of distance from the straits of exit, allow us to estimate the temperature and salinity evolutions as the outflows spread further from their sources
- Second, the vertical profiles are decomposed into components quantifying their salinity vertical gradients and interleaving. These are used to distinguish smooth salinity profiles, indicative of deep continuous flow or submesoscale vortices, from filaments, patches, or lateral injections from layering. These quantities are then correlated with the amplitude of a wavelet power spectrum to estimate the vertical wavelengths
- Third, stability analyses are made to describe the vertical diffusive processes at play when the warm and salty outflows encounter fresher water in the Indian Ocean
- The quantities are mapped and described over the different basins, separating the Gulf of Aden, Gulf of Oman, western Arabian Sea, encompassing the coasts of Yemen, Oman and Somali, and eastern Arabian Sea, encompassing the Indian coast
- Then, we assess the different mechanisms advecting and mixing the salty water masses, from mesoscale and submesoscale perspectives
- Finally, we discuss these results as well as their limitations

2. Data and Methods

2.1. Gathering the Data Sets

As the main objective of this study is to describe the average characteristics of the salty water masses and their variability, we gathered all the vertical profiles of temperature, salinity, and pressure available in the northwestern Indian Ocean. The World Ocean Database (WOD, https://www.nodc.noaa.gov/OC5/WOD/pr_wod.html) provides millions of profiles collected from different devices and quality controlled (Böhme & Send, 2005; Boyer et al., 2009; Owens & Wong, 2009; Wong et al., 2003). Data from the main experiments in the Arabian Sea can be found in this database, for example the International Indian Ocean Expedition (IIOE) (Wyrtki, 1971) up to 1966, the US Joint Global Ocean Flux Study (JGOFS) from 1994 to 1995 (Morrison et al., 1998), Arabesque in 1994 (Burkill, 1999), or the Red Sea Outflow Experiment (REDSOX) (Bower et al., 2005). Added to historical measurements and to more recent experiments, this is the most exhaustive database of individual profiles available. We focus on devices providing measurements of pressure, temperature, and salinity in our region of interest. Our data set includes around 4,000 profiles from the Conductivity-Temperature-Depth (CTD) and expendable CTD casts, about 23,000 moorings from the Ocean Station Data (OSD), and around 55,000 profiles from Profiling Floats (PFLs) such as RAFOS (Rossby et al., 1986), ALACE (Davis et al., 2001), MARVOR (Ollitrault et al., 1994), and PROVOR (Loaec et al., 1998). Argo floats (Argo, 2000) are also included in the WOD, but as these profilers are updated continuously, we choose to download them from the CORIOLIS Data Centre (https://www.coriolis.eu.org) (Gaillard et al., 2009). Over the last two decades, up to December 2018, 539 of them were recorded in our area of interest, increasing our array by about 74,000 profiles flagged as "good."

SeaSoar measurements from the PhysIndien 2011 and 2014 experiments, two surveys conducted by the SHOM in Spring 2011 and 2014 around the Arabian Peninsula are also added to the database. The SeaSoar, an undulating vehicle carrying a CTD, measures the upper 400 m of the water column. This device is subject to biases linked to the thermal inertia of the sensors. These errors are corrected following the methods from Lueck and Picklo (1990) and Mensah et al. (2009), as described in L'Hégaret et al. (2016). Here, each lowering/rising of the vehicle is considered as an individual profile, increasing our database by 9,000 salinity/temperature casts.

The measurement devices which generated our database all have different vertical resolutions and accuracy. Sampling rates of the CTD increased over the decades. The vertical resolution of the measurements depends on the vertical speed of the device, for example, 1 m s^{-1}, up to 3.5 m s^{-1} when mounted on a SeaSoar. The temperature accuracy values from 1×10^{-3}°C to 5×10^{-3}°C, the salinity from 3×10^{-3} to 2×10^{-2} g kg^{-1}, and the pressure from 0.015% to 0.08% depending on the type of instruments (Boyer et al., 2018). The profiling floats, as the CTD, had their accuracy increased over time, from 5×10^{-3}°C to 2×0^{-3}°C in temperature and from 1×10^{-2} to 5×10^{-3} g kg^{-1} in salinity. The salinity measurements from the WOD OSD data set gather automated low-resolution CTD profiles and manual records from salinographs and salinometers. Some

of the profiles were obtained starting 1870s, so one should be cautious with these profiles as the sampling processes and accuracy have evolved over time (see Figure 2b for the yearly distribution of the profiles).

Altogether we obtain a database of more than 165,000 quality checked profiles. Nevertheless, spurious measurements can still sneak in. We removed the obviously wrong records of salinity, temperature, and pressure, exhibiting values above or below the ones observed in the ocean. We took out the profiles localized on land. Each profile showing a difference between two successive vertical measurements above five times the standard deviation of the database and of the local climatology was also discarded. Finally, we removed data obtained from the devices cast into the Red Sea and Persian Gulf as we focus on the salty water masses once they flow out of their basins of generation. The database is then composed of about 126,000 profiles.

Observations are densest in the central Arabian Sea, Gulf of Oman, and Gulf of Aden, with at least 10 profiles per $(1/4°)^2$ bins (Figure 2a). Areas with the lowest concentration of measurements are found further away from the sources of outflows, along the western coast of India and along the equator. The monthly distribution, as shown in Figure 2c, indicates an even division of measurements in the different basins of interest, with the exception of the Gulf of Oman in February, explained by the numerous profiles added from the PhysIndien experiments.

To compute our diagnostics, the profiles are linearly interpolated onto a regular vertical grid with levels every 5 m, from the surface to 2,000-m depth in a similar manner as Chaigneau et al. (2011) and Keppler et al. (2018). As the data sets provide values of practical salinity and in situ temperature, these variables are converted into absolute salinity and conservative temperature *via* the Gibbs SeaWater (GSW) Oceanographic Toolbox of TEOS-10 (https://www.teos-10.org/) (McDougall & Barker, 2011). The potential density σ_0, in situ density ρ, and spiciness are calculated from these vertically interpolated derived quantities.

2.2. Water Masses Detection

PGW and RSW display large variability on the T/S profiles depending on where they are found in the region (Figure 3). As explained in L'Hégaret et al. (2015), the Persian Gulf outflow does not spread on a specific isopycnal, but rather in a range of density. With knowledge of this characteristic, we implement an algorithm detecting the salty water masses, with the least a priori criteria. On a specific isopycnal, salinity and temperature variations compensate each other. Spiciness anomalies act as a passive tracer, not influenced by density variations (Flament, 2002; Tailleux et al., 2005). The detection is performed on the spiciness vertical profiles, using the definition of spiciness from by McDougall and Krzysik (2015) and calculated via the method from Roquet et al. (2015). The lines of constant spiciness are shown by red dotted lines in Figure 4. Spiciness is high for warm and salty waters and decreases as waters get colder and fresher, in other words, the highest values are found in the upper right part of the T/S diagram and the lowest in the lower left part of the figure.

The vertical configuration of a water mass is described here by three positions in density, a maximal peak in spiciness and the two lows, above and below. As shown in Figure 3, three salty water masses are found in our basin of interest: near the surface is the Arabian Sea High Salinity Water (ASHSW) with peaks found between the surface and $\sigma_0 = 25.7$ kg m^{-3} above 200-m depth. This water mass is present all over the region (see Figures 3a–3d) and forms in the northern Arabian Sea near 20°N in winter, and it spreads southward below the surface on the 24 kg m^{-3} σ_0-level (Kumar & Prasad, 1999). Below is the PGW, between $\sigma_0 = 25.5$ kg m^{-3} and 27 kg m^{-3}, and between 120- and 600-m depth. This water mass is mostly observed in the Gulf of Oman, as shown in Figure 3a but also along the western part of the basin, panel c, and even the Gulf of Aden, panel b. More below, the RSW lying between $\sigma_0 = 26$ kg m^{-3} and 28 kg m^{-3}, and between 120- and 1,400-m depth. This water mass is mainly present in the Gulf of Aden, but it also signs along the western part of the basin (see Figures 3b and 3c). These ranges, deduced from Figure 3, include the vertical positions of the lows. They are voluntarily loose to detect the variability of the positions of lows and peaks, but they still correspond to the climatological values of the salty outflow (Prasad et al., 2001; Shetye et al., 1994).

Our algorithm works as follows. As spiciness decreases with depth, each profile is vertically detrended in order to capture where the peak in the water mass is furthest separated from the trend. Without a vertical

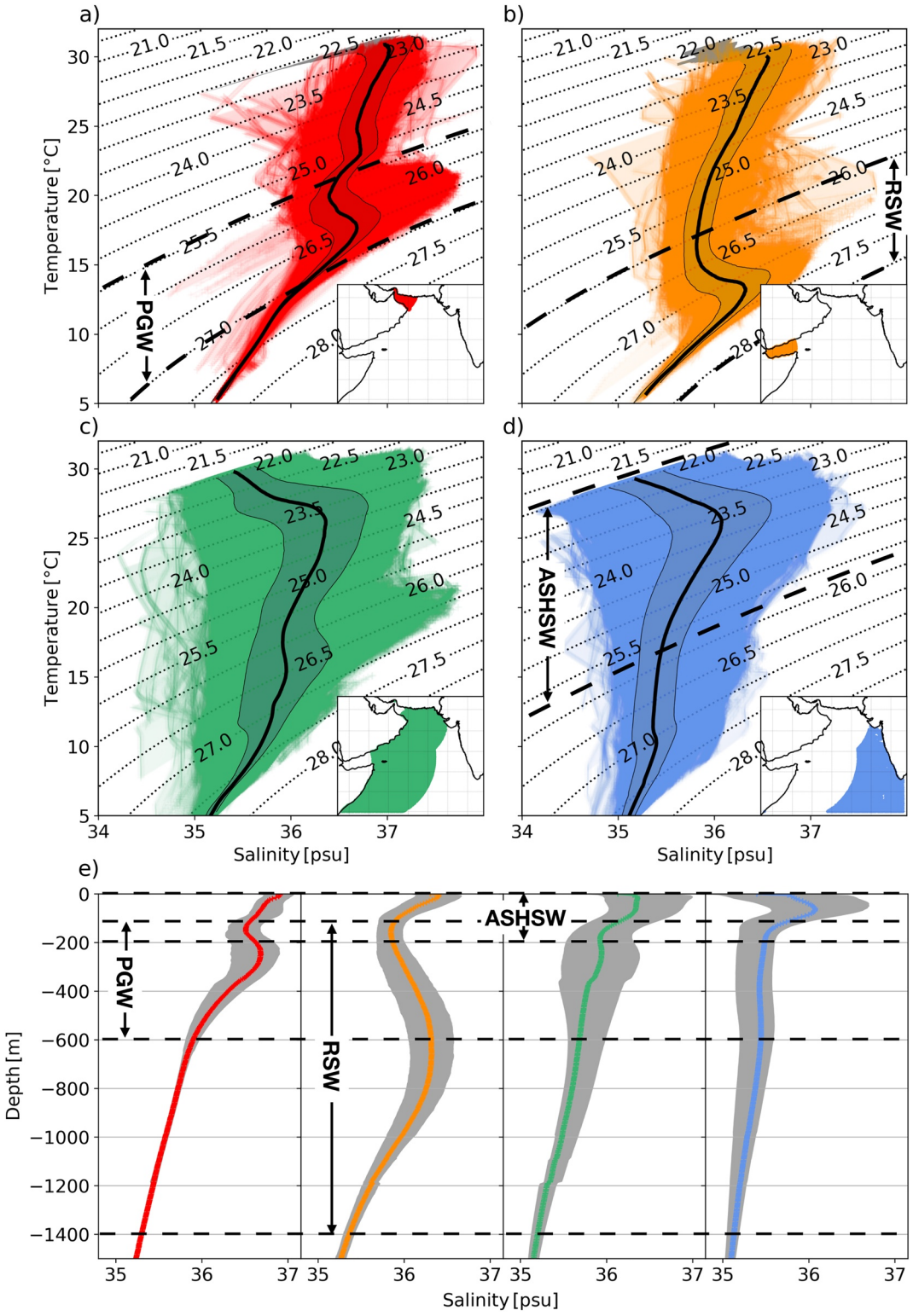

Figure 3. Temperature versus salinity diagram of all profiles (in color) superimposed by the median profile (black line) and standard deviation (shaded area), in the different basins: (a) Gulf of Oman, (b) Gulf of Aden, (c) northwestern Arabian Sea, within 1,700 km from the Strait of Hormuz and 2,500 km from Bab-el-Mandeb, excluding the Gulfs, (d) further offshore in the eastern Arabian Sea. Region highlighted in (c) shows that PGW and RSW still have strong signatures in the northwestern Arabian Sea, while region (d) presents profile with flat signatures. (e) Salinity versus depth diagrams from the same regions. A priori density and depth ranges for each water masses are indicated on the diagrams. PGW, Persian Gulf Water; RSW, Red Sea Water.

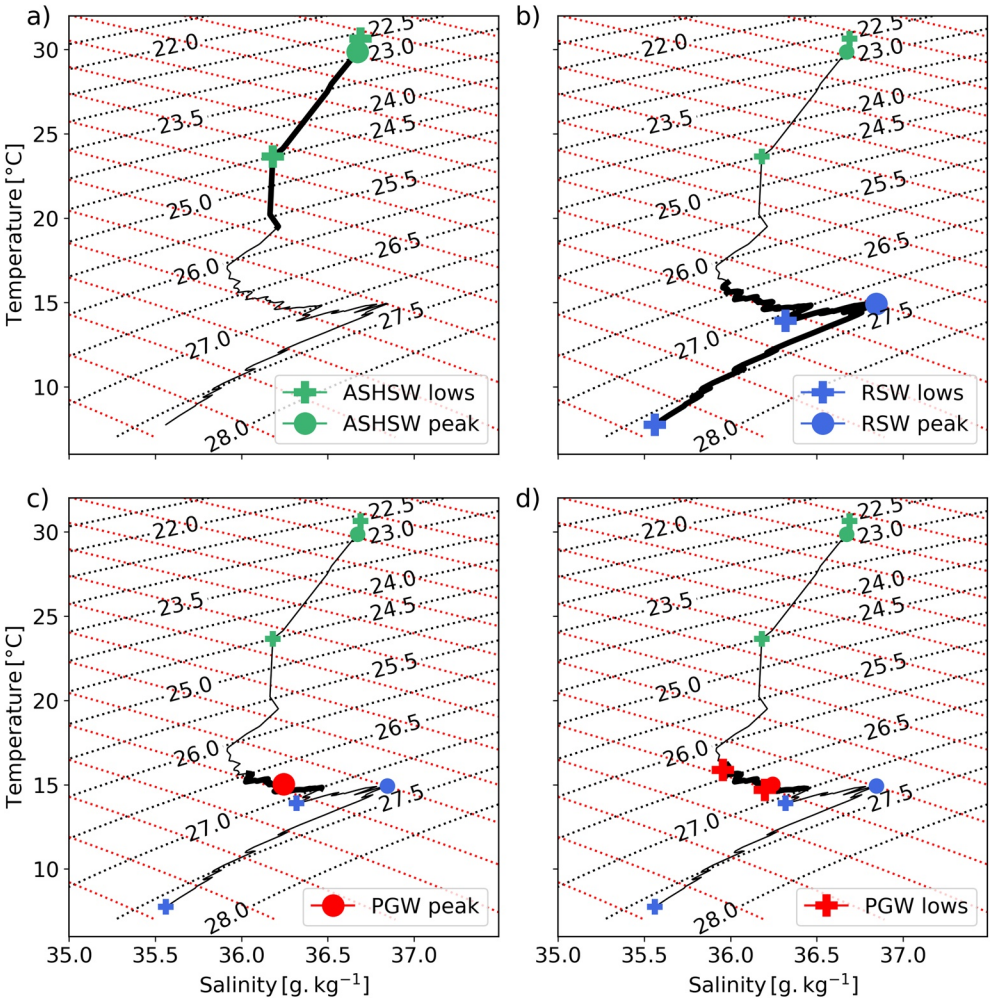

Figure 4. Sketch of the water masses detection by the algorithm. Black and red dotted lines indicate constant density and spiciness, respectively. (a) First, detecting the Arabian Sea High Salinity Water (ASHSW) between the surface and $\sigma_0 = 25.7$ kg m^{-3} and above 200 m depth. This density range is shown by the thicker black portion of the curve. (b) Second, the Red Sea Water (RSW) is found between $\sigma_0 = 26$ kg m^{-3} and 28 kg m^{-3}, and between 120- and 1,400-m depth. (c) Third, the Persian Gulf Water (PGW) peak is captured between the deeper ASHSW low and the upper RSW low, and between 120- and 400-m depth. (d) Fourth, a second round is performed to detect the PGW lows between $\sigma_0 = 25.5$ kg m^{-3} and 27 kg m^{-3} in density, and in the 120–600 m depth range.

detrending, a profile capturing a diluted outflow with a weak signature could not be detected because of the surrounding stratification.

First, it detects the ASHSW. The spiciness curve is reduced to a portion comprised between the surface and the density 25.7 kg m^{-3} (Figure 4a shows this profile on a T/S diagram, with the corresponding portion underlined with a thicker black line). Along this profile, the vertical positions of the lows in spiciness for the uppermost and lowermost portions are found above and below $\sigma_0 = 25.2$ kg m^{-3} and saved. It corresponds to the two green crosses in Figure 4a. The original curve is then reduced to a new portion comprised between the two minima and the position of the peak is recorded (green dot in Figure 4a).

Second, the algorithm detects the RSW. In the same manner, as for the ASHSW, the profile is sectioned to a portion comprised with the a priori densities of the RSW $\sigma_0 = 26$–28 kg m^{-3}, with the two lows found above and below $\sigma_0 = 27.2$ kg m^{-3} (Figure 4b). Another criterion is added to avoid sampling PGW: the RSW bottom low must be found below 600-m depth (Bower et al., 2000; Prasad et al., 2001).

Third, it detects a salinity peak found by partitioning the spiciness curve from the positions previously calculated, between the ASHSW bottom low and the RSW upper low (thick black curve on Figure 4c) and between 150- and 400-m depth. Finally, PGW lows are located above and below this peak, in the range of $\sigma_0 = 25.5$–27 kg m^{-3}, and in the 120–600 m depth range (corresponding to the thick black curve on Figure 4d). The detection of the PGW and RSW uses two criteria, the one based on density and the other on depth because they can be found in similar density ranges, thus ensuring a better distinction between the two salty outflows.

Some vertical profiles, particularly for the PGW and RSW outflows, display layering with numerous peaks. In these situations, the selected peak is the furthest separated from the trend.

2.3. Stratification, Stability, and Dilution

To determine if the salty outflow is either vertically structured as a smooth, deep continuous flow, or rather layered with fresher water being injected inside its core, we decompose the salinity S into two components: $\overline{S}$ the low-pass filtered salinity using a Butterworth filter with a cutoff frequency set at $\sigma_0 = 0.2$ kg m^{-3}, and $S' = S - \overline{S}$.

Considering the quantity:

$$\left|\partial_\sigma \overline{S_{\text{outflow}}}\right| = \frac{1}{\Delta\sigma_{\text{outflow}}} \int_{\sigma_-}^{\sigma_+} \left|\partial_\sigma \overline{S}\right| d\sigma,$$

with $\Delta\,\sigma_{\text{outflow}} = \sigma_+ - \sigma_-$ where σ_+ and σ_- are the two densities encompassing the core of a water mass, $_{\text{outflow}}$ subscript corresponds to the outflow name, either $_{\text{PGW}}$ or $_{\text{RSW}}$, and || denotes the absolute value. This quantity provides the absolute average of the low-pass filtered salinity gradient, equivalent to the diapycnal gradient. Large values correspond to a profile presenting a peak in salinity (see Figure 5a) while values close to zero hints toward a flat profile (see Figure 5b). For each water mass, $\left|\partial_\sigma \overline{S_{\text{PGW}}}\right|$ and $\left|\partial_\sigma \overline{S_{\text{RSW}}}\right|$ are large near their basins of formation and decrease with distance as they are diluted. Nevertheless, we can expect the regional distribution of these variables to be modified by the mesoscale circulation.

The vertical profiles often present several peaks and lows in salinity inside the same water masses. To quantify this layering, we define:

$$\left|S'_{\text{outflow}}\right| = \frac{1}{\sigma_{\text{outflow}}} \int_{\sigma_-}^{\sigma_+} \left|S'\right| d\sigma,$$

equivalent to the standard deviation of salinity anomalies compared to the low-pass filtered one, averaged in the outflow density range. Large values of $|S'_{\text{PGW}}|$ and $|S'_{\text{RSW}}|$ underline the difference between the measured profile and the filtered one, indicating the lateral injection of saltier or fresher waters (see Figure 5c). Values close to zero, oppositely, are indicative of similar measured and filtered profiles, as shown in Figure 5d. Finally, negative and positive values of S'_{outflow} indicate that the outflow respectively loses and gains salinity through the mixing process.

The mixing and advection processes induce vertical variability in the outflows at specific wavelengths. To quantify them, the salinity profiles are decomposed using a continuous wavelet transform (or CWT). The square root of normalized wavelet power spectrum for each vertical wavelength is obtained via:

$$\hat{S}_{\text{outflow}}(\lambda_z) = \frac{1}{\Delta\sigma_{\text{outflow}}} \int_{\sigma_-}^{\sigma_+} \sqrt{S_w S_w^*}\, d\sigma,$$

with S_w the continuous wavelet transform, S_w^* its complex conjugate, and λ_z the vertical wavelength. The correlation coefficient was computed at every vertical wavelength between this term and the previously mentioned components of salinity profiles $\left(\left|S'_{\text{outflow}}\right| \text{ and } \left|\partial_\sigma \overline{S_{\text{outflow}}}\right|\right)$, which is denoted as $\text{Corr}\left(\left|S'_{\text{outflow}}\right|, \hat{S}_{\text{outflow}}(\lambda_z)\right)$

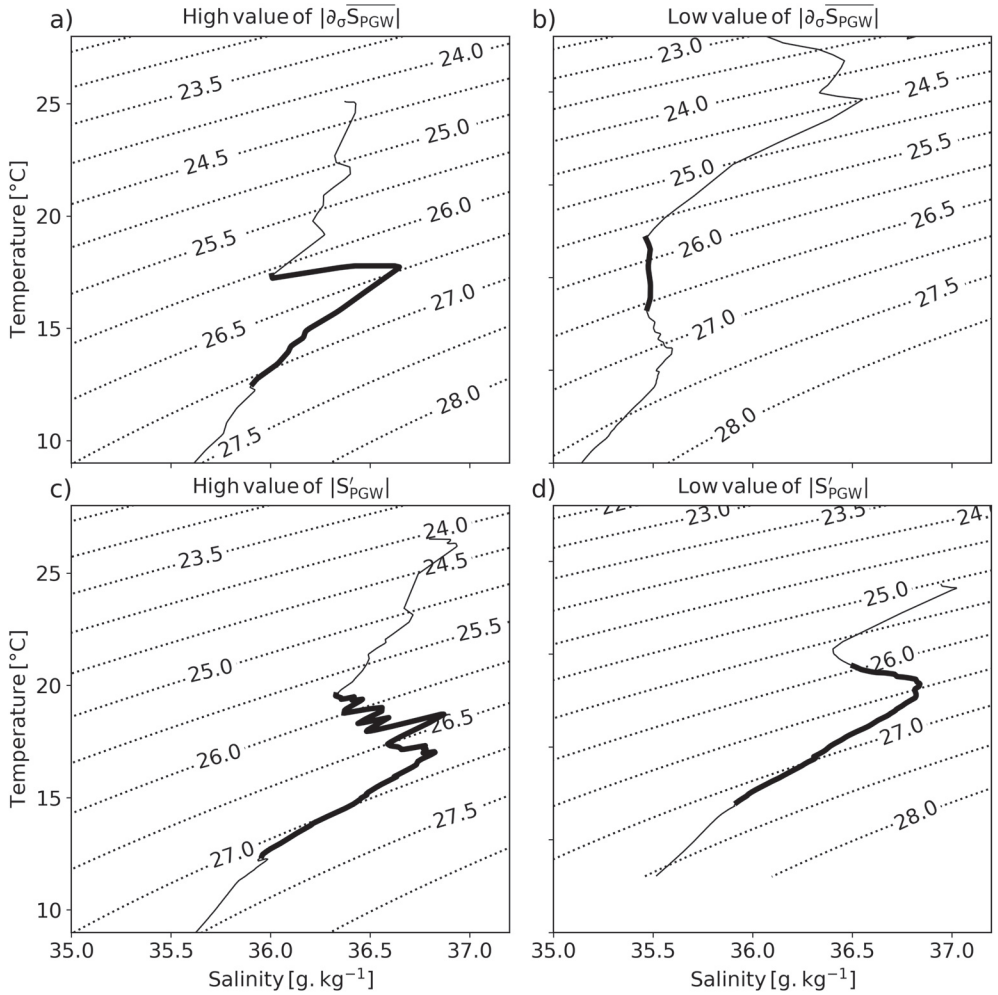

Figure 5. An example of temperature and salinity diagram for (a) large and (b) small low-pass filtered salinity gradient, $\left|\partial_\sigma \overline{S_{PGW}}\right|$. The values of $\left|\partial_\sigma \overline{S_{PGW}}\right|$ are 1.22 g m^3 kg^{-2} for panel (a) and 0.04 g.m^3 kg^{-2} for panel (b). (c and d) same as (a and b), but for $|S'_{PGW}|$, which is a measure of interleaving. The values of $|S'_{PGW}|$ is 4.22 and 0.99 g kg^{-1} for panels (c and d), respectively. PGW, Persian Gulf Water; RSW, Red Sea Water.

or $\mathrm{Corr}\left(\left|\partial_\sigma \overline{S_{\mathrm{outflow}}}\right|, \hat{S}_{\mathrm{outflow}}(\lambda_z)\right)$. This quantity is used hereafter to understand the vertical scales observed in the profiles, the width variability of the outflow core, and of the interleaving.

In the Arabian Sea, the outflows enter a well-stratified upper ocean, injecting salty and warm waters into the thermohaline structure, possibly leading double diffusive instability (Azizpour et al., 2017). Stability properties can be estimated by the density ratio (Turner, 1979) defined as

$$\mathrm{R}_\rho = \frac{\alpha \partial \mathrm{T} / \partial Z}{\beta \partial \mathrm{S} / \partial Z}$$

with α and β the thermal expansion and haline contraction coefficients, respectively, and Z depth. To increase readability, Ruddick (1983) introduces the Turner angle, defined as

$$\mathrm{Tu} = \tan^{-1} \frac{R_\rho - 1}{R_\rho + 1}$$

We will use Tu hereafter to describe double diffusive processes. $-90° < Tu < -45°$ indicates stable diffusive convection, warm and salty waters are found below colder and fresher waters (below −90° it is unstable), $45° < Tu < 90°$ underlines the presence of warm and salty waters above colder and fresher ones, favorable conditions for salt fingering (above 90° the stratification is unstable), and $-45° < Tu < 45°$ a doubly stable water column. Figure 3 in You (2002) presents a clear illustration of the density ratio and Turner angle.

Away from their basins of formation, the outflows are expected to present eroded salinity peaks, where double diffusive processes are less efficient. In their Appendix B Yeager and Large (2004) link vertical diffusivity of salinity and temperature to R_ρ. To quantify the double diffusion processes for profiles with a distinct salinity signature, we selected only those having a vertical diffusivity and a $\left|\partial_\sigma \overline{S_{\text{outflow}}}\right|$ above their median value in the Arabian Sea.

In summary, from the vertical salinity profiles, four quantities are calculated over the density ranges of the outflow. The Turner Angle Tu suggests the presence of double diffusive processes. Hereafter it is calculated from the upper low to the peak of the outflow, and from the peak to the bottom low. The vertical dyapicnal gradient, that can be viewed as the intensity of the salinity peak, is quantified by $\left|\partial_\sigma \overline{S_{\text{outflow}}}\right|$, and the layering by $\left|S'_{\text{outflow}}\right|$. The combination of both these terms is used in the next section to better understand the regional configurations of the outflow vertical structures. Finally, the correlation between these terms and $\hat{S}_{\text{outflow}}(\lambda_z)$, obtained by a CWT, highlights the wavelength on which these structures appear.

3. Results

3.1. Spreading of the Water Masses

3.1.1. Persian Gulf Outflow

The salty outflows occupy all the water columns in the Persian Gulf and Red Sea. When they exit their basins of formation, they first cascade down, stabilize at their neutral buoyancy depth, and spread toward the open Indian Ocean. Figures 6 and 7 display the spatial distribution and variability of these spreads.

From the Gulf of Oman to about 2,500-km offshore, the average thermohaline characteristics are calculated by averaging the measurements in 25-km bins, equidistant from the Strait of Hormuz (red curves on Figures 6c–6e). From this local average, we calculate the difference between the maximal salinity detected on each profile and the mean. Figure 6b shows these anomalies and provides information on the local variability and differences found between two neighboring profiles. In terms of potential density, the PGW peak is found between 26.4 and 26.7 kg m^{-3} in the Gulf of Oman and western Arabian Sea with an average value increasing of 1 kg m^{-3} from west to east. Potential density then decreases when reaching the eastern Arabian Sea with peaks found down to 25.8 kg m^{-3} and its mean value decreasing by 1.5 kg m^{-3}. Figures 6c and 6d show that PGW undergoes an exponential decrease of temperature and salinity with distance, from, on average, 37 to 35 g kg^{-1} and 20°C–13°C. From this pattern, the Gulf of Aden arises as an exception. There, the detected water masses present higher salinity than the one observed for the PGW in the western Arabian Sea, with a larger density. This might be due to the fact that the detection algorithm did not detect only PGW, but also RSW cascading down in the PGW range of density, thus increasing salinity in this layer. It also suggests that a portion of the RSW spreads in a layer with lighter density with peaks found above the usual value of 27 kg m^{-3}.

The local variability of the PGW thermohaline characteristics is also consistent with dilution; from the western Gulf of Oman, the standard deviation of salinity decreases from 0.3 to less than 0.1 g kg^{-1} with distance (Figure 6c). Similarly, the measurements range over 1.5 g kg^{-1} near the Strait of Hormuz to less than 0.5 g kg^{-1}. Note that while standard deviation of salinity decreases with distance, standard deviation of temperature remains constant with distance from the strait, with a value of about 1.2°C (Figure 6d).

Figure 6b shows the salinity anomaly, calculated as a difference between the measurements and the average salinity function of distance from the Strait of Hormuz (Figure 6c). As expected, the highest variability is found in the Gulf of Oman (leaving aside the Gulf of Aden). South of 10°N, a positive salinity PGW anomaly is found from the coast of Somalia to 60°E, whereas in the eastern Arabian Sea the anomaly tends toward

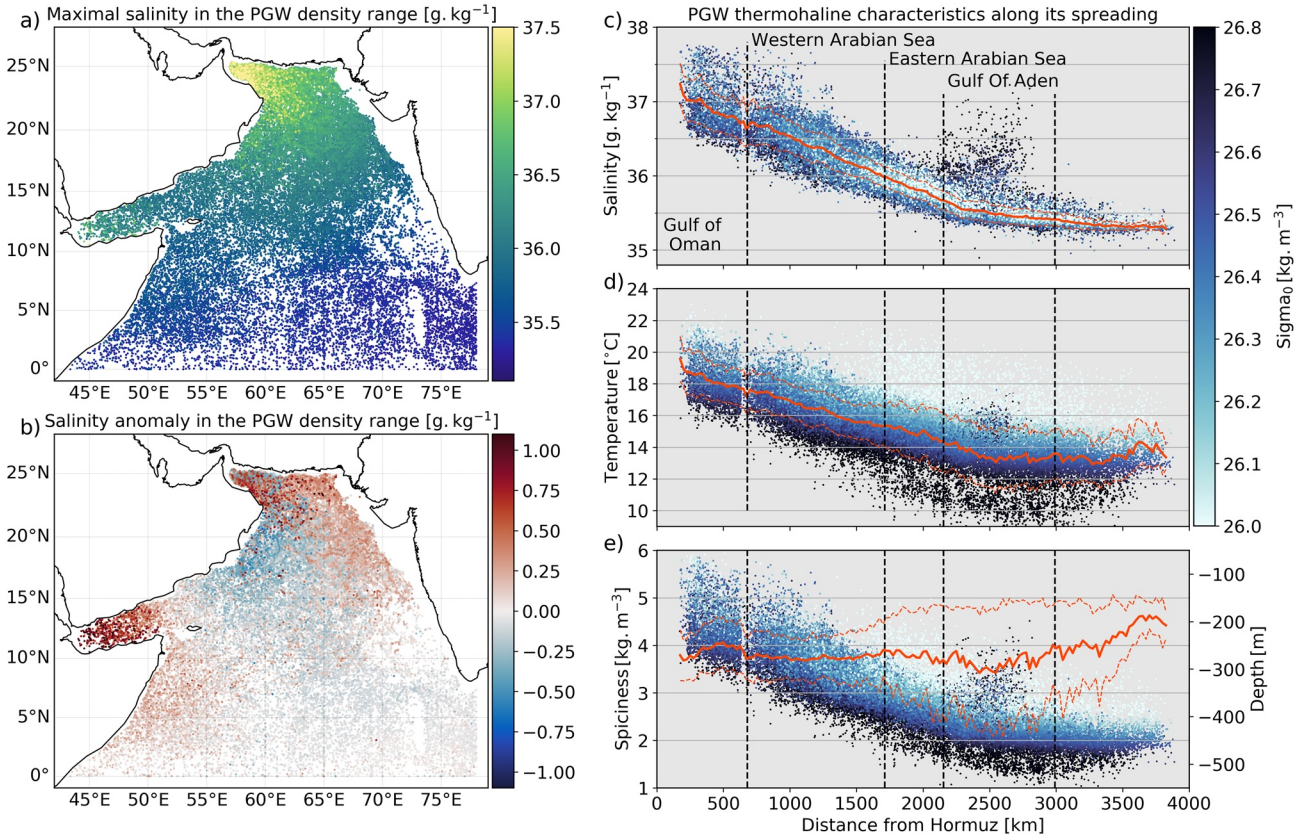

Figure 6. (a) Maximal salinity in the PGW layer detected by the algorithm. (b) Salinity anomaly calculated between the maximal PGW salinity and the average salinity field against the distance from the Strait of Hormuz (red curve on top panel c). (c–e) From top to bottom, distribution of salinity, temperature, and spice at the PGW salinity peak against distance from the Strait of Hormuz. Potential density σ_0 where the peak is detected is color-coded. Red curve on top and middle panels corresponds to the median salinity and temperature distribution in 25-km bins, and the dashed curves indicate the standard deviations from these medians (Figure 7). Red curves on the bottom panel indicate the median depth of the PGW salinity peak. PGW, Persian Gulf Water; RSW, Red Sea Water.

zero. This zonal difference is linked to the entrance of Bay of Bengal water from the east, mixing PGW with fresher water via lateral mixing (Prasad et al., 2001; Shetye et al., 1991). Far from its source, the PGW layer becomes shallower (see red line in Figure 6e) which is coherent with previous observations in the eastern Abarian Sea (Shankar et al., 2005; Shenoi et al., 2005). In this region, the salinity of the PGW does not span over a wide ranges but is found around 35.2 g kg^{-1}, and all the variability in density can be linked to changes in temperature (see Figures 6c and 6d).

3.1.2. Red Sea Outflow

The RSW outflow salt and heat loss undergoes three different phases along its path (Figure 7c). From the Strait of Bab-el-Mandeb to about 1,500-km downstream (down to Socotra), this outflow loses salinity by 1 g kg^{-1} on average, from 36.5 to 35.5 g kg^{-1}, and heat by 3°C, from 14°C to 11°C. There, the RSW displays large density values, around 27.2 kg m^{-3}, the salinity varying over a range of 0.8 g kg^{-1}, with a standard deviation of 0.2 g kg^{-1}. Figure 7b shows that this variability is spread fairly uniformly across the Gulf of Aden.

While entering the Arabian Sea, the salt and heat dilution reduces, as the salinity and temperature remain constant. Over this region, the amplitude in salinity and temperature variability range over 1 g kg^{-1} and 5°C, respectively. This variability is shown in Figure 7b. Highest salinity values are found in the northern Arabian Sea while lower ones are found between the equator and 10°N. This indicates that the outflow keeps a stronger signature in the northern and eastern portion of the basin, while the southwestern one is more diluted. This implication of a southward motion of the RSW along the Indian coast is consistent with the observations from Shankar et al. (2005) and Shenoi et al. (2005). This boundary at 10°N is also present in the seasonal variability (Figure 8b), with the exception of a few isolated saltier measurements along the Somali

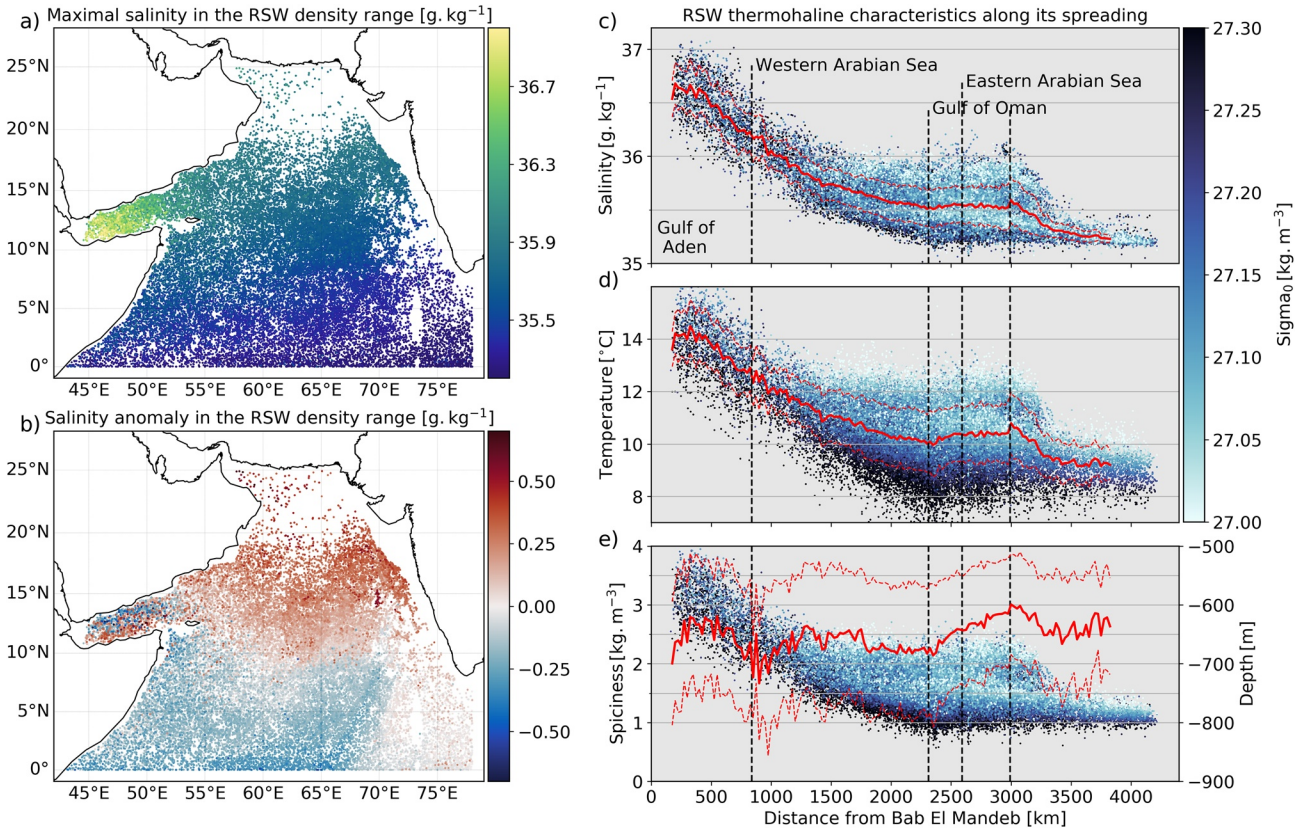

Figure 7. (a) Maximal salinity in the RSW layer detected by the algorithm. (b) Salinity anomaly calculated between the maximal RSW salinity and the average salinity field against the distance from Bab-el-Mandeb (red curve on top panel c). (c–e) From top to bottom, distribution of salinity, temperature, and spice at the RSW salinity peak against distance from Bab-el-Mandeb. Potential density σ_0 where the peak is detected is color-coded. Red curve on top and middle panels corresponds to the median salinity and temperature distribution in 25-km bins, and the dashed curves indicate the standard deviations from these medians. Red curves on the bottom panel indicate the median depth of the RSW salinity peak. RSW, Red Sea Water.

coast in winter. There, the RSW pathway is influenced by the seasonal surface circulation. In summer, this separation between the low and high salinity values is located at the northern boundary of the cross-equatorial clockwise gyre described in Jensen (2003) and L'Hégaret et al. (2018), extending to 70°E. Along the coast of Somalia, this gyre is comprised of the northward Somali Current and Great Whirl, whose barotropic signature (Beal & Donohue, 2013) suggests strong mixing at depth and few direct exchanges between the Gulf of Aden and Somali Basin during this season. In winter, the RSW along the coast of Somalia is advected across the equator southward within the Somali Undercurrent (Beal et al., 2000).

Finally, RSW is seldom found north of 20°N and in the Gulf of Oman. RSW detected north of 20°N has salinity values above 36.2 g kg^{-1}; from Figure 7c, we estimate that they match densities around 26.9 kg m^{-3} and depths between 400 and 500 m (not shown). The thermohaline characteristics as a function of distance (Figures 7c and 7d) display a localized gain of heat and salt in the Gulf of Oman. In this basin, the PGW maximal salinity signature is found at 26.6 kg m^{-3} in density and between 160- and 310-m depth (Figure 6c). Nevertheless, a thick outflow could reach deeper layers via diffusive processes or eddy stirring. This situation underlines the necessity to better describe the vertical structure of the outflows, which is the subject of the next section.

3.2. Vertical Structure

Along their paths from the straits to the southern Arabian Sea, the outflows are diluted, losing salt and heat. Their vertical structures provide useful information on the mechanisms responsible for their dilution. First, we need to quantify the vertical coherence of the core of the outflow. To do so, a low-pass filter is applied to

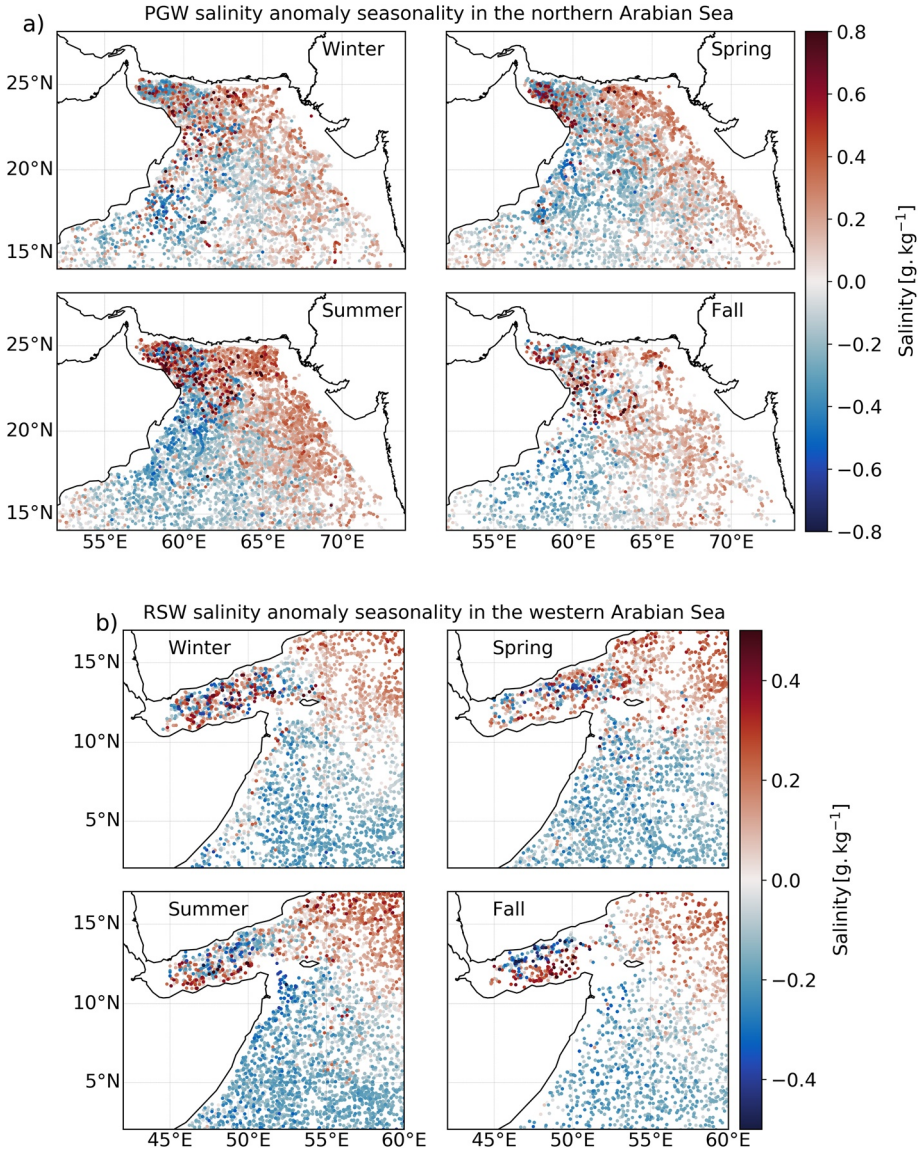

Figure 8. Seasonality of the salinity anomalies calculated between the maximal measured salinity in the outflow density range and the average salinity function of the distance (red curves from Figures 6c and 7c). Names correspond to the boreal seasons. (a) PGW salinity anomaly in the northern part of the Arabian Sea. (b) RSW salinity anomaly in the western part of the Arabian Sea. PGW, Persian Gulf Water; RSW, Red Sea Water.

the salinity profiles, using a Butterworth filter with a cutoff frequency set at $\sigma_0 = 0.2$ kg m^{-3}. Then the absolute value of the salinity gradient is averaged between the two local lows above and below its peak $\left|\partial_\sigma \overline{S_{\text{outflow}}}\right|$. For readability, this quantity is normalized by its average value in the Arabian Sea. Profiles with values above one underline the presence of a salty core clearly distinguishable from its background environment, whereas profiles with values below one tend to be flat. This quantity is mapped on Figures 9a and 10a for the PGW and RSW.

The distribution of $\left|\partial_\sigma \overline{S_{\text{outflow}}}\right|$ as a function of salinity and distance (top panels Figures 9a and 10a) underlines the correlation between a coherent core and a strong peak in salinity, particularly near the straits.

The absolute difference between the measured profile S and the filtered one $\overline{S}$ is then averaged over the outflow density range $\left|S'_{\text{outflow}}\right|$. This quantity can be linked to layering. Figures 9b and 10b exhibit the standard

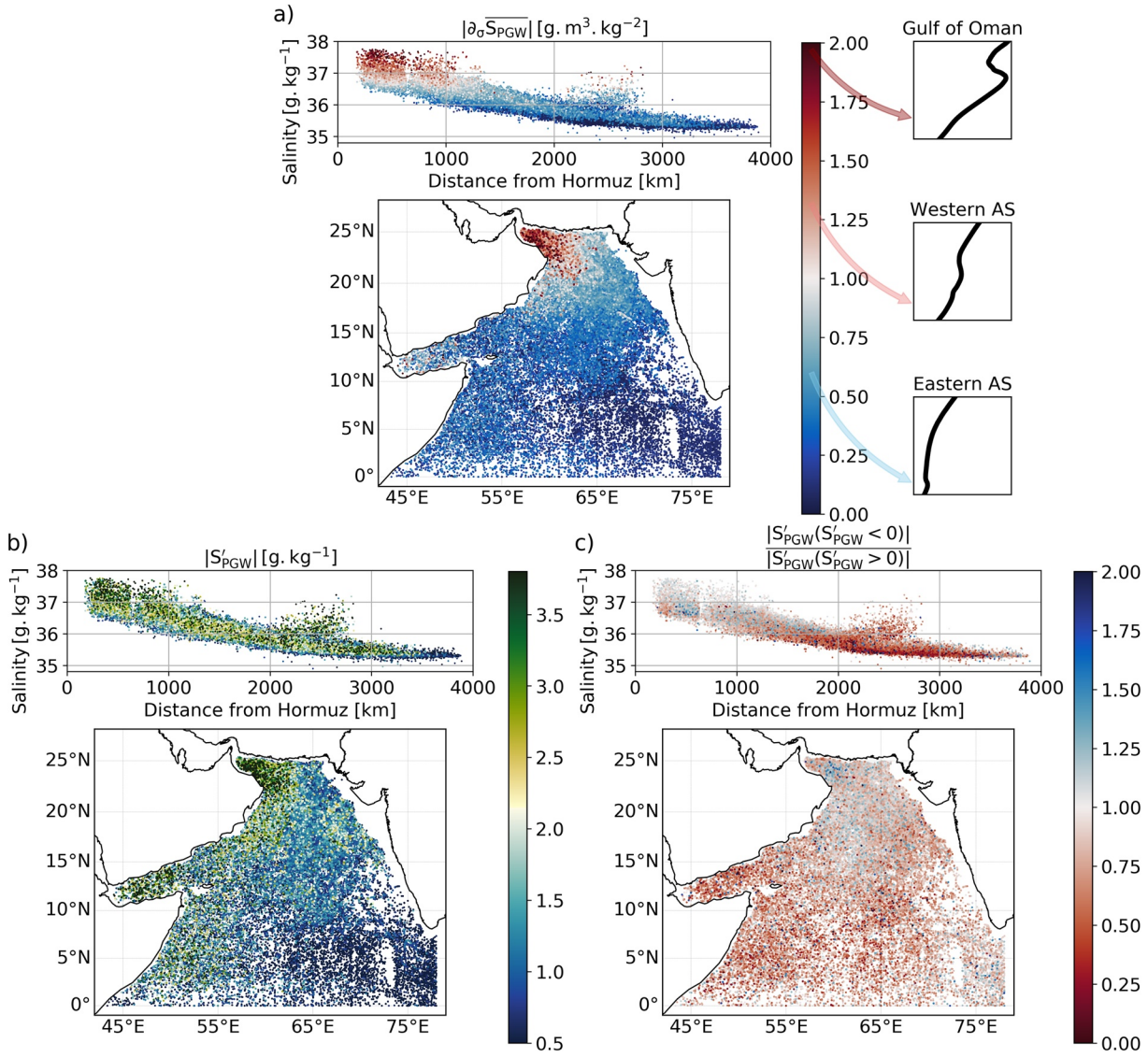

Figure 9. Vertical structure of the PGW layer. (a) Average of the absolute low-pass filtered vertical salinity gradient over the PGW outflow width. Temperature versus salinity profiles averaged over the regions shown in Figure 3 are shown along the color bar. (b) Absolute value of S'_{PGW}, calculated as the difference between the measured salinity profile and the low-pass filtered one, averaged over the PGW outflow width. (c) Ratio of negative S'_{PGW} (fresh water) over positive one (salty water). PGW, Persian Gulf Water.

deviation of salinity anomalies compared to the low-pass filtered one; the ratio of $\left|S'_{outflow}\right|(S'_{outflow} < 0)$ over $\left|S'_{outflow}\right|(S'_{outflow} > 0)$, respectively indicating lateral injection of fresher and saltier waters, is shown in Figures 9c and 10c.

The highest $\left|\partial_\sigma \overline{S_{PGW}}\right|$ values are found between the Strait of Hormuz and 20°N (see Figure 9a), but both flat and steep profiles are observed. Out of the Gulf of Oman, the peaking signatures quickly diminish. Isolated peaking profiles are found along the western coast of the Arabian Sea rather than on the eastern part of the basin (Figure 9a). Similar to the thermohaline characteristics, some isolated salinity peaks are observed in the Gulf of Aden. Finally, flatter than average profiles are found in a southwest/northeast band, from the coast of Somalia to the northwestern coast of India, south of 15°N extending toward the equator. This is expected as the outflow dilutes as it is further away from its source. Flat profiles are also dominant between 50°E and 55°E, enclosed between Socotra and Yemen.

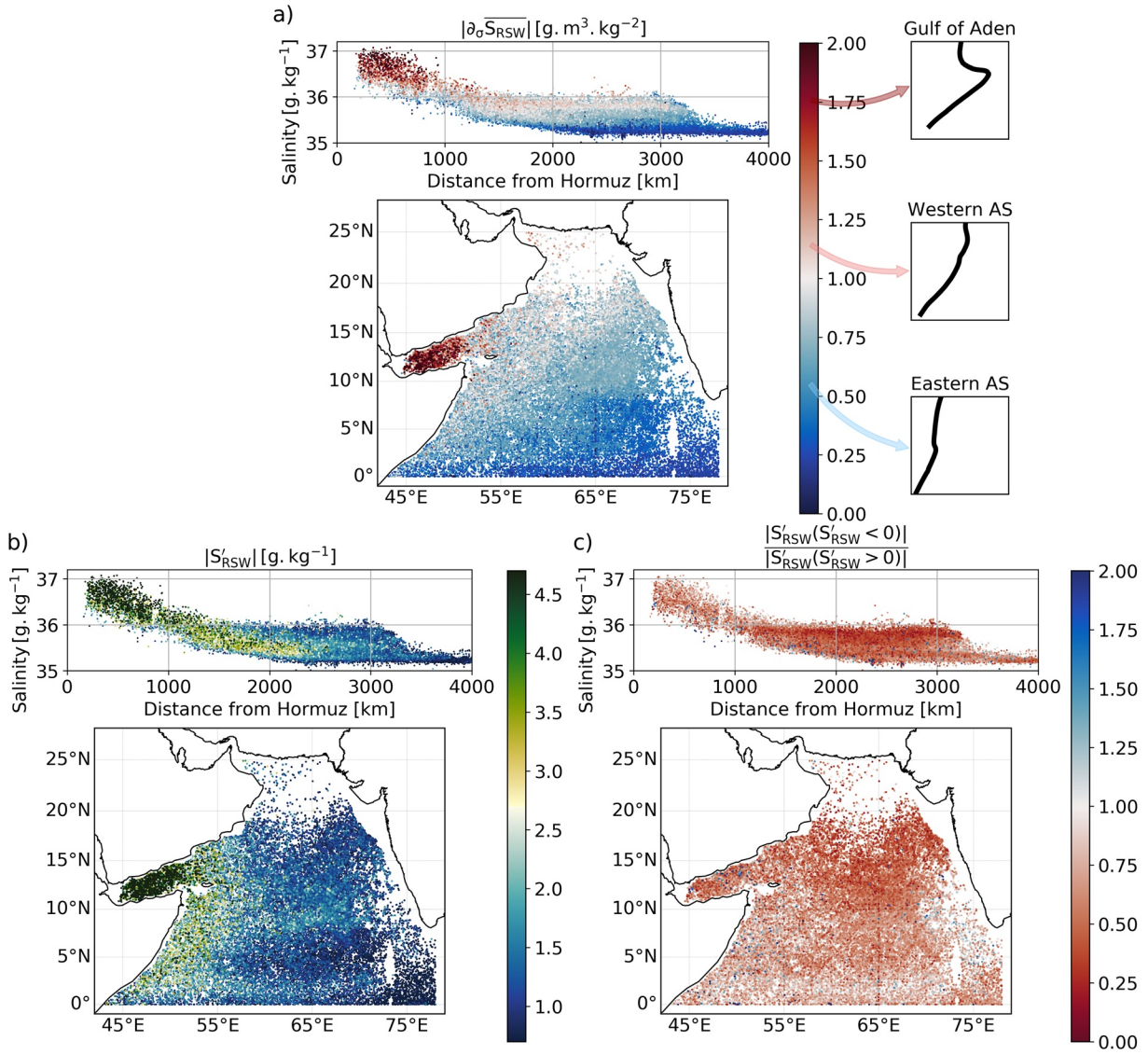

Figure 10. Vertical structure of the RSW layer. (a) Average of the absolute low-pass filtered vertical salinity gradient over the RSW outflow width. Temperature versus salinity profiles averaged over the regions shown in Figure 3 are shown along the color bar. (b) Absolute value of S'_{RSW}, calculated as the difference between the measured salinity profile and the low-pass filtered one, averaged over the RSW outflow width. (c) Ratio of negative S'_{RSW} (fresh water) over positive one (salty water). RSW, Red Sea Water.

The region with large $\left|S'_{PGW}\right|$ (as shown in Figure 9b), which represents interleaving, is quite similar to $\left|\partial_\sigma \overline{S_{PGW}}\right|$ with one notable exception along the coast of Somalia and offshore. There, above average layering is observed within the Great Whirl influence region and such profiles are observed in Beal and Donohue (2013). All along the northwestern Arabian Sea, which is a region filled with mesoscale eddies, the layering is above average.

In the Gulf of Oman, the presence of flat profiles in the distribution of PGW as a function of salinity (top panel Figure 9a) indicates that offshore, well-mixed, water are advected westward. As observed in Figure 9b (top panel), these profiles near the Strait of Hormuz and with low salinity present also a low $|S'_{PGW}|$, meaning that the interleaving is weak. Such profiles indicate that this fresh water mass is advected within the core of the coherent structures, such as mesoscale eddies or submesoscale lenses (Morvan et al., 2019). Furthermore, the presence of water masses with different thermohaline characteristics in a turbulent area, lead to strong interleaving. Figure 9b indeed shows the presence of high $|S'_{PGW}|$ from the Gulf of Oman to

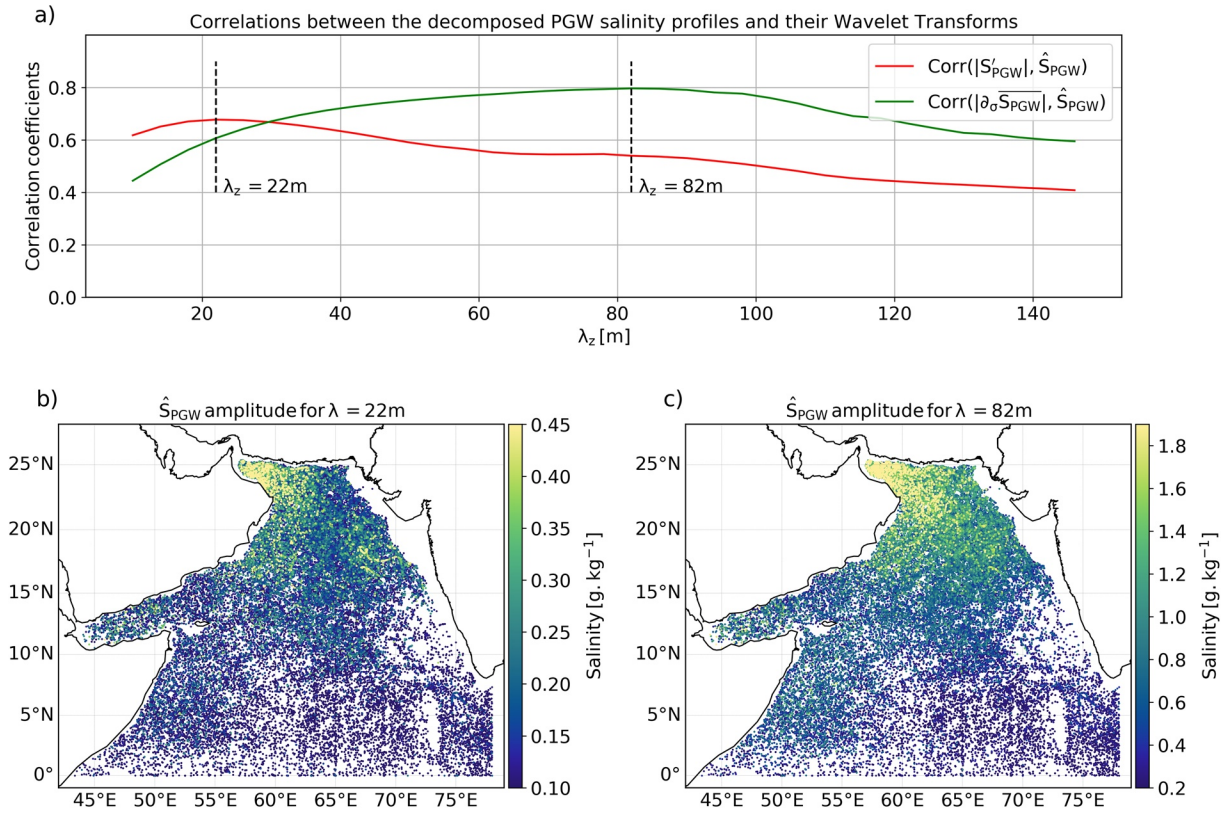

Figure 11. Wavelet analysis of the PGW layer. Correlation coefficients calculated at each vertical wavelength, from the amplitude of the salinity wavelet power spectrum $\hat{S}$ (a) Correlations between $\hat{S}$ and low-pass filtered profiles $|S'_{PGW}|$ (red line) and with the salinity gradients of the vertical profiles $\left|\partial_\sigma \overline{S_{PGW}}\right|$ (green line). These quantities are integrated over the width of the PGW layer. Maximal correlation coefficients are indicated with the black dashed line, and the associated spatial configuration of $\widehat{S_{PGW}}(\lambda_z)$ for these specific wavelengths are shown in (b and c). PGW, Persian Gulf Water.

the western coast of the Arabian Sea, extending south to 15°N, injecting both fresh and salty water in the Gulf of Oman (see Figure 9c). Further southwest, the layering is intensified in the Gulf of Aden and along the coast of Somalia. Figure 11a shows that a high correlation (around 0.7) is found between $|S'_{PGW}|$ and vertical salinity variability, centered around a vertical wavelength of 22 m. As shown in Figure 11b, the lateral injections observed in the Gulf of Oman and north of 15°N in the Arabian Sea have width around 20 m. In the same region (Figure 11c), the PGW core is showing large variability with vertical scales ranging from 30 to 150 m, with a maximal correlation centered at 82 m.

The RSW outflow slopes underlined by $\left|\partial_\sigma \overline{S_{RSW}}\right|$ shows the highest value in the Gulf of Aden (Figure 10a). There, the vast majority of the profiles sampled in the Gulf of Aden exhibits high values of $\left|\partial_\sigma \overline{S_{RSW}}\right|$. Along a southwest-northeast band stretching from the coast of Somalia to the northern Arabian Sea, steeper than average profiles are measured and distributed over this area. Compared to the PGW, the RSW keeps a stronger peak in salinity, even 3,000 km away from its source and along the Indian coast (see Figure 10a, top panel).

Important interleaving measured by $|S'_{RSW}|$ is observed in the Gulf of Aden (as shown in Figure 10b), leading to salty injections toward the surrounding waters (Figure 10c). Contrary to the Gulf of Oman, we observe that fresh water is not entrained in the western Gulf of Aden; almost all profiles show a large peak in salinity $\left|\partial_\sigma \overline{S_{RSW}}\right|$ and strong layering $|S'_{RSW}|$ (see Figures 10a and 10b, top panels). Another important difference from the PGW is that the wavelet analysis reveals that the layering operates on a much wider vertical wavelength range (see Figure 12a). For vertical wavelengths between 50 and 200 m, the correlation

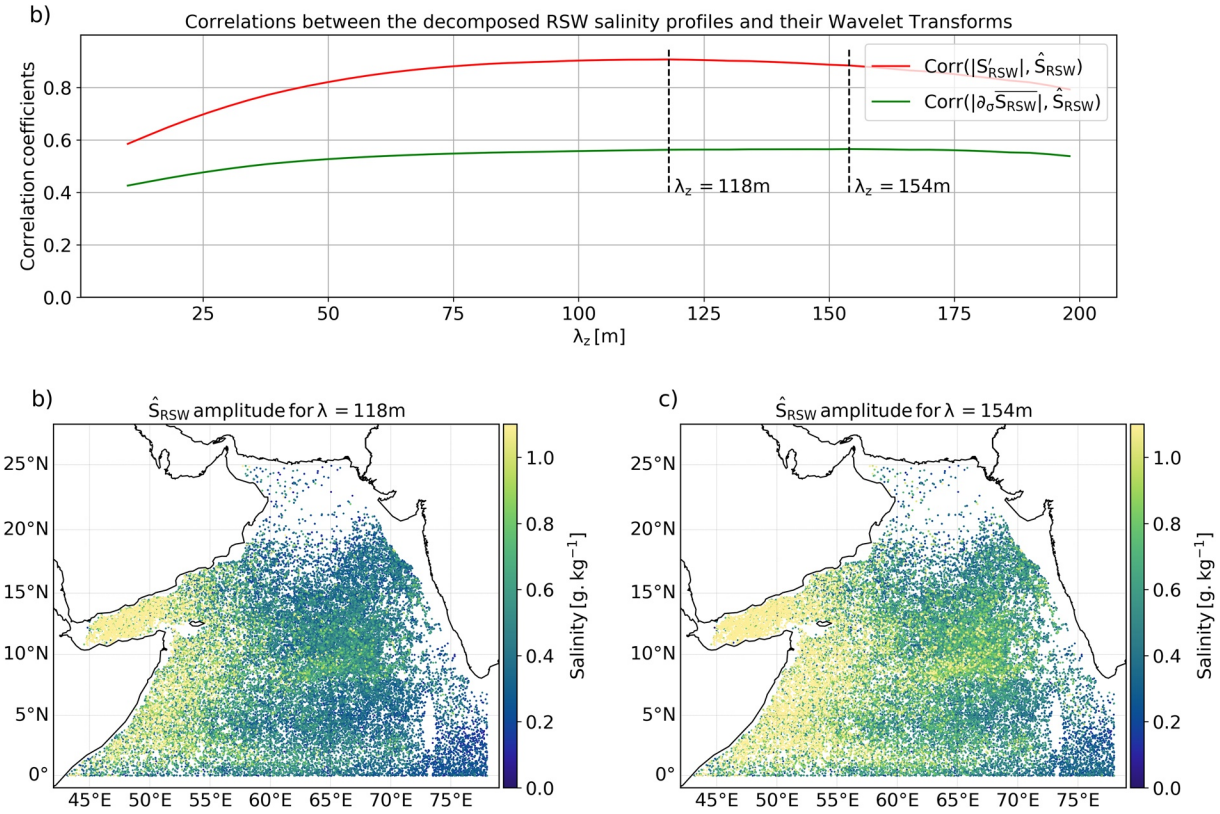

Figure 12. Wavelet analysis of the RSW layer. Correlation coefficients calculated at each vertical wavelength, from the amplitude of the salinity wavelet power spectrum $\hat{S}$ (a) Correlations between $\hat{S}$ and low-pass filtered profiles $|S'_{RSW}|$ (red line) and with the salinity gradients of the vertical profiles $\left|\partial_\sigma \overline{S_{RSW}}\right|$ (green line). These quantities are integrated over the width of the PGW layer. Maximal correlation coefficients are indicated with the black dashed line, and the associated spatial configuration of $\widehat{S_{RSW}}(\lambda_z)$ for these specific wavelengths are shown in (b and c). PGW, Persian Gulf Water; RSW, Red Sea Water.

coefficients are above 0.8. It is more difficult to find a specific wavelength for the core of the RSW as correlations are high over a wide range; maximal correlation is found around 150 m.

Some isolated profiles with strong $\left|\partial_\sigma \overline{S_{RSW}}\right|$ are shown in Figure 10a, around Socotra and along the Somali coast. Such signatures in a region far from the outflow source are characteristic of submesoscale vortices trapping RSW, such as the ones described in Shapiro and Meschanov (1991). After exiting the Gulf of Aden, the water mass with these structures is advected in a basin filled with intense mesoscale eddies inducing shear, thus breaking these lenses (Morvan et al., 2019). Most of them are observed west of 60°E, but some are found flowing along the coast in the Somali undercurrent during the winter monsoon and reaching the Mozambique Channel (Beal et al., 2000).

4. Mixing and Advection Mechanisms

4.1. Double Diffusive Regimes

In their study of the western Gulf of Oman, Ghazi et al. (2016) showed that the upper boundary of the outflow is in favorable condition for diffusive convection, with warmer waters found below colder ones, while the lower boundary is in both diffusive convection and salt fingering favorable conditions. Extending this approach to the whole Arabian Sea and to both the PGW and RSW outflows, we see that they have similar behaviors. Here, we present only profiles with above average vertical diffusivity for salinity to remove the eroded ones.

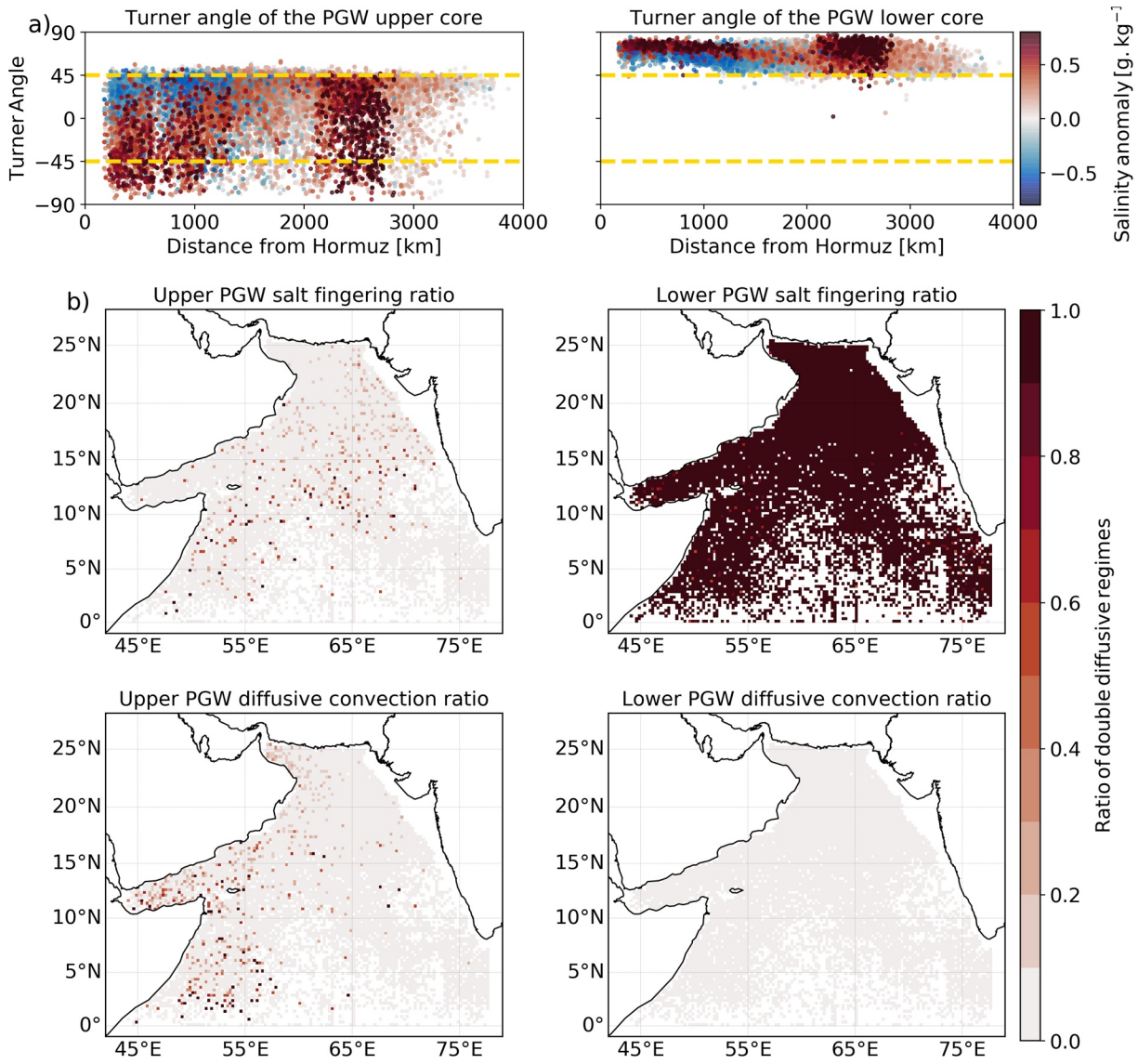

Figure 13. Double diffusive regimes for the PGW outflow. The outflow is divided into two parts, an upper one from the upper lows to the peaks in the temperature versus salinity profiles (left panels) and a second from the peaks to the lower lows (right panels). (a) Distribution of the Turner angle relative to distance, with in color the salinity anomaly calculated between the peak value in the PGW density range and the average salinity distribution function of the distance from the strait of exit (red curves from Figure 6c). Values above 45 are indicative of salt fingering favorable regime, and below −45 of diffusive convection favorable regime. (b) Ratio of the number of profiles per 0.25° bins in salt fingering (upper panels) and diffusive convection (lower panels) favorable conditions. PGW, Persian Gulf Water.

A straightforward result observed in Figures 13b and 14b (top left panels) for both the outflows is that their lower cores are in favorable conditions for salt fingering. This is expected as these salty outflows encounter fresh water masses along their lower boundaries. Their upper cores are subject to diffusive convection in the same areas where the layering shows high values, with higher ratios found in the western parts of the Gulf of Oman and the Gulf of Aden (see Figures 13 and 14). This is particularly important for the upper boundary of the RSW outflow in the Gulf of Aden, where up to 80% of the profiles are in favorable diffusive convection regime.

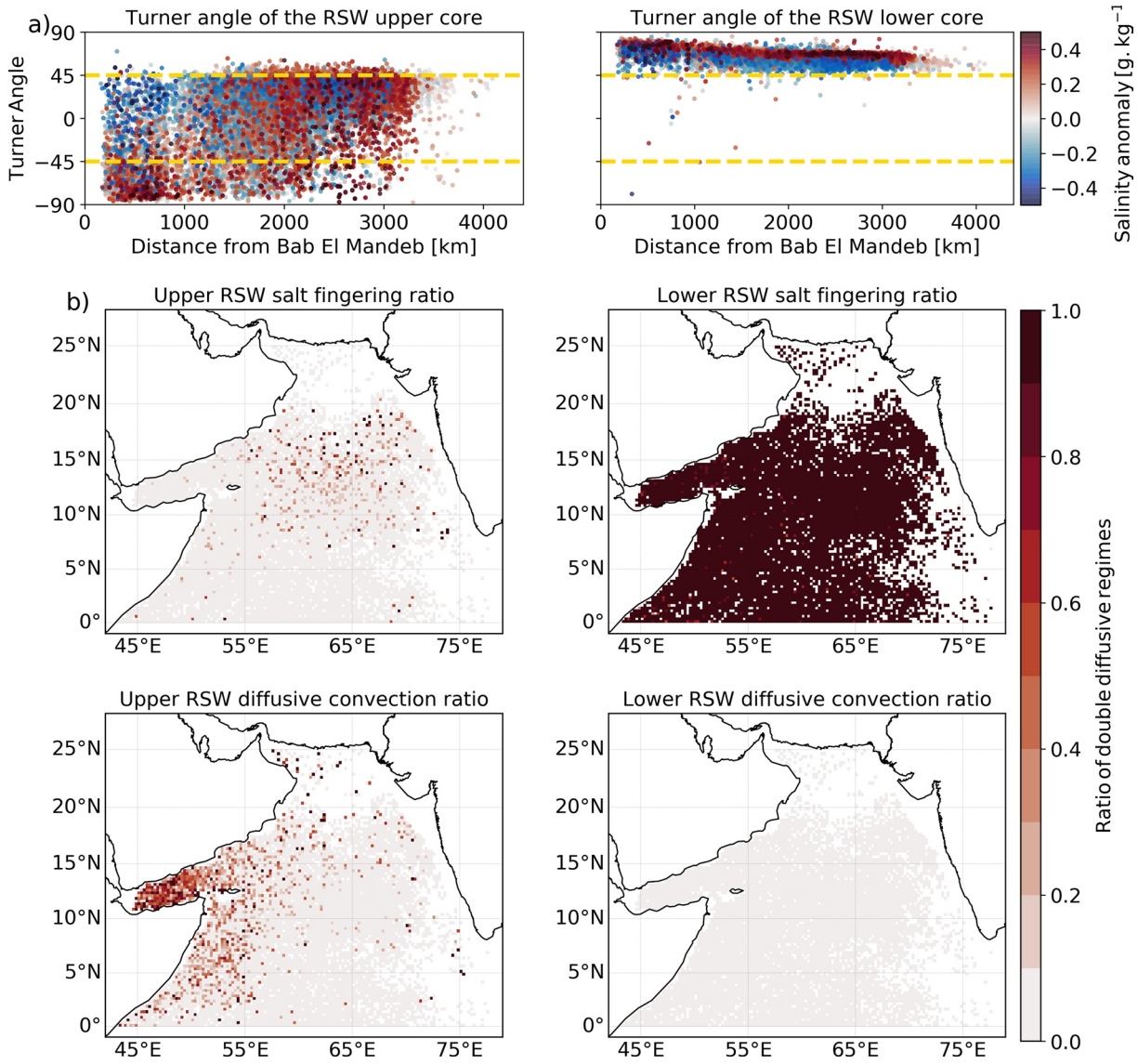

Figure 14. Double diffusive regimes for the RSW outflow. The outflow is divided into two parts, an upper one from the upper lows to the peaks in the temperature versus salinity profiles (left panels) and a second from the peaks to the lower lows (right panels). (a) Distribution of the Turner angle relative to distance, with in color the salinity anomaly calculated between the peak value in the RSW density range and the average salinity distribution function of the distance from the strait of exit (red curves from Figure 6c). Values above 45 are indicative of salt fingering favorable regime, and below −45 of diffusive convection favorable regime. (b) Ratio of the number of profiles per 0.25° bins in salt fingering (upper panels) and diffusive convection (lower panels) favorable conditions. RSW, Red Sea Water.

4.2. Turbulent Mixing

4.2.1. Mesoscale Eddies

In the western Arabian Sea, south of Ra's al-Hadd, the PGW presents lower salinity values, while in contrast, higher salinity values are found along the northeastern edge of the basin (see Figure 6b). Figure 8a shows that this asymmetry exists no matter the season, even if the PGW spread is highly seasonal, as described in Prasad et al. (2001).

An explanation for this east/west asymmetry in local salinity anomalies could be linked to transit time. The longer the water mass is separated from its formation region, the more it will experience dilution processes. The salinity anomaly presented in Figure 6b is calculated by averaging all the profiles found within a certain distance from the Strait of Hormuz, not the real distance the water parcels crossed. Higher salinity peak is

observed in the eastern basin, which hints toward a more direct path for the PGW, while the profiles found near the western boundary might sample PGW layers that have been traveling in the basin for a longer period. However, Schmidt et al. (2019) stated that transit time is shorter to the western part than to the eastern part of the Arabian Sea.

Another explanation for this east/west asymmetry can be related to turbulent mixing, as thin layers are rapidly vertically homogenized. Layers with vertical wavelengths around 20 m for the PGW and between 50 and 200 m for the RSW (see Figures 11 and 12) can be attributed to stirring by mesoscale eddies (Smith & Ferrari, 2009), to stirring via submesoscale eddies shear, or to near-inertial wave shear (Jaeger et al., 2020). Without observing a time evolution of the structure or their horizontal structures, it is difficult to assess which mechanism is at play. Nonetheless, we know that the western part of the Arabian Sea is a region with an intense mesoscale eddy activity.

Kim et al. (2001) stated that the EKE increases in the western and southwestern Arabian Sea and is relatively weaker in the northern and eastern portions of the basin. Furthermore, the spatial distribution of $|S'_{PGW}|$ exhibits the same patterns as the eddy detection from Trott et al. (2018). As described in L'Hégaret et al. (2015), the surface mesoscale eddies have a strong impact at depth, dominating the circulation, primarily in the upper 500 m depth (Pegliasco et al., 2015), and at depth, they wrap the outflows into filaments around them and stir the different water masses (Ilıcak et al., 2011; Vic et al., 2015). The PGW advected in such a turbulent field is thus much subject to dilution. As it reaches a region with less active mesoscale eddies, the PGW layer can retain more marked thermohaline characteristics while flowing eastward along the Arabian Peninsula, then undergoing less dilution processes.

4.2.2. Diapycnal Mixing in the Gulfs

The thermohaline characteristics of the PGW and RSW, shown in Figures 6c and 7c, indicate the relative contribution of temperature and salinity to the water mass stability. The temperature field shows a stable stratification, with heavier water corresponding to cold water and vice versa. Nevertheless, the salinity field exhibits an unorganized stratification. There, the potential density variability is mainly dominated by the salinity.

From the Strait of Hormuz to 1,300 km downstream for the PGW, the outflows are unstable. As shown in the spiciness diagram (Figures 6e and 7e), heavier and lighter PGW and RSW peaks occur on a wide range of temperature and salinity. This spice variability is indicative of diapycnal mixing (Todd et al., 2012). Different mechanisms can lead to such mixing in the gulfs. In their early evolutions, the outflows cascade down and equilibrate with surrounding waters, inducing strong changes in the water mass depth (as shown by the red curves from Figures 6e and 7e. Along their paths in the Gulfs of Oman and Aden, the outflows are advected at the rim of mesoscale eddies (Al Saafani et al., 2007; Bower & Furey, 2012), interacting with the topographic slopes. Along the coast, they induce small-scale lateral diapycnal fluxes creating cross isopycnal motions (Colas et al., 2013). The interaction between eddies and the topography generates internal waves, enhancing diapycnal mixing (Whalen et al., 2012). In the Arabian Sea, this situation is observed near the Murray Ridge at 20°N (Quraishee, 1984). Finally, as stated in Morvan et al. (2019), the shear instability created along the coasts of the Gulfs form submesoscale eddies.

5. Discussion

Using all available historical thermohaline measurements, we develop a detection algorithm allowing us to capture the vertical characteristics of the salty outflows in the Arabian Sea. The salinity peaks are encapsulated between two local vertical lows. With these outflow layers, we are able to calculate two metrics, one quantifying the intensity of the salinity gradients and one quantifying the interleaving. These quantities are mapped in the northwestern Indian Ocean and with the distance from their straits.

The PGW and RSW outflows undergo similar processes across the Arabian Sea. In the first phase, these water masses lose salt and heat in the Gulfs of Oman and Aden, from which they outflow. In these basins the outflow signatures stand out with sharp vertical salinity gradients. Nevertheless, the water masses are subject to mixing induced by the interaction with the topography and with mesoscale eddies, or by submesoscale structures, as pointed out by the strong interleaving observed there. The flow is then easily

broken into smaller fragments. We observe an exponential loss of salt and heat along these basins, and only a few recordings show a high salinity peak outside of these basins. This is particularly observed for the RSW outflow, whereas the PGW outflow can be advected further offshore while keeping more pronounced salinity peaks. Vice versa, fresher waters originated from the Arabian Sea rarely reach the western Gulf of Aden.

Out of the Gulfs of Oman and Aden, the number of profiles with high salinity peaks is limited, marking the start of the second phase for the outflows' evolution. Mesoscale eddies are vigorous near the western boundary of the Arabian Sea, injecting PGW and RSW by lateral mixing in the water column (A. S. Fischer et al., 2002; L'Hégaret et al., 2016; Resplandy et al., 2011), and the interaction between the eddies and the topography lead to the formation of submesoscale structures and internal waves. This region is characterized by strong interleaving. For the PGW outflow, these lateral injections operate at vertical wavelengths between 20 and 50 m, while it is much larger, between 75 and 150 m, for the RSW outflow. This process reduces the salinity and temperature of the outflows, particularly for the PGW as it is advected at shallower depth than the RSW, more impacted by the mesoscale eddies. Co-localized with these lateral mixing regions, the outflows upper cores are in favorable conditions for diffusive convection, potentially losing heat toward the upper water column. During these first two phases, the outflows exhibit a seasonal variability, linked to the surface currents and mesoscale eddies.

When reaching the eastern Arabian Sea, the outflows present more homogeneous characteristics, with thinner layers and reduced range of potential densities. All over our region of interest, we observe that the lower cores of the outflows are in favorable salt fingering conditions. Nevertheless, we must point out that we are not following the outflows along their actual pathways, since we do not have information on the time they spent in the Arabian Sea. Instead, we are assessing their characteristics with distance from the straits where they outflow. The decay in salinity, temperature, and spiciness that we observe with distance is different from the actual diffusivity of the outflows.

From these spatial distributions, we can conclude that the PGW outflow remains a deep continuous flow only in the western Gulf of Oman; downstream, it interacts with turbulent processes, such as the mesoscale eddies, stirring the outflow and mixing it with surrounding waters. When arriving in the open Arabian Sea, these processes continue, and only a few profiles still present a coherent core. Submesoscale lenses, such as the one measured in Senjyu et al. (1998) and L'Hégaret et al. (2016) are thus only expected to be observed in the early stages of the PGW outflow, north of 20°N and west of 65°E. It is also important to underline that fresher waters are also stirred around the eddies and are entrained into the western Gulf of Oman.

This study hints toward the fact that mesoscale eddies have a huge impact on the outflows characteristics, mixing, and advection. These interactions are also different if the outflow is stirred at the periphery of these structures or captured inside their cores. As we can now co-localize mesoscale eddies from satellite measurements (Chaigneau et al., 2011; de Marez et al., 2019; Le Vu et al., 2018) with in situ observation, further observational studies should focus on the link between these structures and water masses evolution. While the altimetry resolution is not submesoscale resolving, a large vertical salinity gradient, associated with a small standard deviation between the salinity profile and the low-pass filtered one, found at the periphery of an eddy could be indicative of the presence of a submesoscale coherent vortex. These structures are key in spreading the water masses, as they have been shown to impact the vertical mixing of another salty outflow from the Mediterranean Sea (Bosse et al., 2015; Meunier et al., 2015). Furthermore, we only used temperature, salinity, and density here, but we should use in situ velocity measurements as well to increase the understanding on the diffusive processes at play in the real ocean.

Through this study we have shown that:

- In the Gulfs of Oman and Aden and in the western Arabian Sea, the salty outflows show strong interleaving, leading to a loss of heat and salt along the flow path in the basins
- This loss is likely linked to lateral mixing processes, particularly the interaction between mesoscale eddies and the regional topography
- In the eastern Arabian Sea, the salty water masses present more homogeneous characteristics, with low interleaving and flat salinity profiles
- Highly saline structures are rarely observed outside of the Gulfs

Data Availability Statement

Data can be accessed here https://www.nodc.noaa.gov/OC5/WOD/pr_wod.html. The authors are also grateful to the Coriolis Data Centre, handling operational oceanography measurements made in situ, complementing the measurement of the ocean surface made using instruments aboard satellites. Data can be accessed here https://www.Coriolis.eu.org. The data sets from PhysIndien 2011 and 2014 can be accessed on the SEANOE website https://doi.org/10.17882/77351 for 2011 and https://doi.org/10.17882/77355 for 2014. The authors thank the reviewers for their in-depth analyzes of the manuscript, as well as their suggestions and comments, which helped to increase its quality.

Acknowledgments
The authors thank the World Ocean Database (WOD), a collection of scientifically quality-controlled ocean profile data, an NCEI product and an International Oceanographic Data and Information Exchange (IODE) project, funded in partnership with the NOAA OAR Ocean Observing and Monitoring Division.

References

Al Saafani, M., Shenoi, S., Shankar, D., Aparna, M., Kurian, J., Durand, F., & Vinayachandran, P. (2007). Westward movement of eddies into the Gulf of Aden from the Arabian Sea. *Journal of Geophysical Research: Oceans*, *112*(C11). https://doi.org/10.1029/2006jc004020

Argo (2000). *Argo float data and metadata from Global Data Assembly Centre (Argo GDAC)*. SEANOE.

Azizpour, J., Chegini, V., & Siadatmousavi, S. M. (2017). Seasonal variation of the double diffusion processes at the strait of Hormuz. *Acta Oceanologica Sinica*, *36*(1), 26–34. https://doi.org/10.1007/s13131-017-0990-6

Beal, L. M., & Donohue, K. A. (2013). The Great Whirl: Observations of its seasonal development and interannual variability. *Journal of Geophysical Research: Oceans*, *118*(1), 1–13. https://doi.org/10.1029/2012jc008198

Beal, L. M., Ffield, A., & Gordon, A. L. (2000). Spreading of Red Sea overflow waters in the Indian Ocean. *Journal of Geophysical Research*, *105*(C4), 8549–8564. https://doi.org/10.1029/1999jc900306

Böhme, L., & Send, U. (2005). Objective analyses of hydrographic data for referencing profiling float salinities in highly variable environments. *Deep Sea Research Part II: Topical Studies in Oceanography*, *52*(3–4), 651–664. https://doi.org/10.1016/j.dsr2.2004.12.014

Bosse, A., Testor, P., Mortier, L., Prieur, L., Taillandier, V., d'Ortenzio, F., & Coppola, L. (2015). Spreading of levantine intermediate waters by submesoscale coherent vortices in the northwestern Mediterranean Sea as observed with gliders. *Journal of Geophysical Research: Oceans*, *120*(3), 1599–1622. https://doi.org/10.1002/2014jc010263

Bower, A. S., & Furey, H. H. (2012). Mesoscale eddies in the Gulf of Aden and their impact on the spreading of Red Sea outflow water. *Progress in Oceanography*, *96*(1), 14–39. https://doi.org/10.1016/j.pocean.2011.09.003

Bower, A. S., Hunt, H. D., & Price, J. F. (2000). Character and dynamics of the Red Sea and Persian Gulf outflows. *Journal of Geophysical Research*, *105*(C3), 6387–6414. https://doi.org/10.1029/1999jc900297

Bower, A. S., Johns, W. E., Fratantoni, D. M., & Peters, H. (2005). Equilibration and circulation of Red Sea outflow water in the Western Gulf of Aden. *Journal of Physical Oceanography*, *35*(11), 1963–1985. https://doi.org/10.1175/jpo2787.1

Boyer, T. P., Antonov, J. I., Baranova, O. K., Garcia, H. E., Johnson, D. R., & Mishonov, A. V. (2009). *World ocean database 2009*.

Boyer, T. P., Baranova, O. K., Coleman, C., Garcia, H. E., Grodsky, A., & Locarnini, R. A. (2018). *World ocean database 2018*.

Burkill, P. (1999). Arabesque: An overview. *Deep Sea Research Part II: Topical Studies in Oceanography*, *46*(3–4), 529–547. https://doi.org/10.1016/s0967-0645(98)00116-7

Cember, R. P. (1988). On the sources, formation, and circulation of Red Sea deep water. *Journal of Geophysical Research*, *93*(C7), 8175–8191. https://doi.org/10.1029/jc093ic07p08175

Chaigneau, A., Le Texier, M., Eldin, G., Grados, C., & Pizarro, O. (2011). Vertical structure of mesoscale eddies in the eastern South Pacific Ocean: A composite analysis from altimetry and Argo profiling floats. *Journal of Geophysical Research*, *116*(C11). https://doi.org/10.1029/2011jc007134

Chang, Y. S., Özgökmen, T. M., Peters, H., & Xu, X. (2008). Numerical simulation of the Red Sea outflow using HYCOM and comparison with REDSOX observations. *Journal of Physical Oceanography*, *38*(2), 337–358. https://doi.org/10.1175/2007jpo3697.1

Colas, F., Capet, X., McWilliams, J. C., & Li, Z. (2013). Mesoscale eddy buoyancy flux and eddy-induced circulation in eastern boundary currents. *Journal of Physical Oceanography*, *43*(6), 1073–1095. https://doi.org/10.1175/jpo-d-11-0241.1

Davis, R. E., Sherman, J. T., & Dufour, J. (2001). Profiling ALACES and other advances in autonomous subsurface floats. *Journal of Atmospheric and Oceanic Technology*, *18*(6), 982–993. https://doi.org/10.1175/1520-0426(2001)018<0982:paaoai>2.0.co;2

de Marez, C., Carton, X., Corréard, S., L'Hégaret, P., & Morvan, M. (2020). Observations of a deep submesoscale cyclonic vortex in the Arabian Sea. *Geophysical Research Letters*, *47*(13), e2020GL087881. https://doi.org/10.1029/2020gl087881

de Marez, C., l'Hégaret, P., Morvan, M., & Carton, X. (2019). On the 3D structure of eddies in the Arabian Sea. *Deep Sea Research I: Oceanographic Research Papers*, *150*, 103057.

Durgadoo, J. V., Rühs, S., Biastoch, A., & Böning, C. W. B. (2017). Indian ocean sources of Agulhas leakage. *Journal of Geophysical Research: Oceans*, *122*(4), 3481–3499. https://doi.org/10.1002/2016jc012676

Fischer, A. S., Weller, R. A., Rudnick, D. L., Eriksen, C. C., Lee, C. M., Brink, K. H., et al. (2002). Mesoscale eddies, coastal upwelling, and the upper-ocean heat budget in the Arabian Sea. *Deep Sea Research Part II: Topical Studies in Oceanography*, *49*(12), 2231–2264. https://doi.org/10.1016/s0967-0645(02)00036-x

Fischer, J., Schott, F., & Stramma, L. (1996). Currents and transports of the Great Whirl-Socotra Gyre system during the summer monsoon, August 1993. *Journal of Geophysical Research*, *101*(C2), 3573–3587. https://doi.org/10.1029/95jc03617

Flament, P. (2002). A state variable for characterizing water masses and their diffusive stability: Spiciness. *Progress in Oceanography*, *54*(1–4), 493–501. https://doi.org/10.1016/s0079-6611(02)00065-4

Gaillard, F., Autret, E., Thierry, V., Galaup, P., Coatanoan, C., & Loubrieu, T. (2009). Quality control of large Argo datasets. *Journal of Atmospheric and Oceanic Technology*, *26*(2), 337–351. https://doi.org/10.1175/2008jtecho552.1

Ghazi, E., Bidokhti, A. A., Ezam, M., Azad, M. T., & Hassanzadeh, S. (2016). Physical properties of Persian Gulf outflow thermohaline intrusion in the Oman Sea. *Open Journal of Marine Science*, *7*(1), 169–190.

Ilıcak, M., Özgökmen, T. M., & Johns, W. E. (2011). How does the Red Sea outflow water interact with Gulf of Aden eddies? *Ocean Modelling*, *36*(1–2), 133–148.

Jaeger, G. S., Lucas, A. J., & Mahadevan, A. (2020). Formation of interleaving layers in the Bay of Bengal. *Deep Sea Research Part II: Topical Studies in Oceanography*, *172*, 104717.

Jensen, T. G. (2003). Cross-equatorial pathways of salt and tracers from the northern Indian ocean: Modelling results. *Deep Sea Research Part II: Topical Studies in Oceanography*, *50*(12–13), 2111–2127. https://doi.org/10.1016/s0967-0645(03)00048-1

Keppler, L., Cravatte, S., Chaigneau, A., Pegliasco, C., Gourdeau, L., & Singh, A. (2018). Observed characteristics and vertical structure of mesoscale eddies in the Southwest Tropical Pacific. *Journal of Geophysical Research: Oceans*, *123*(4), 2731–2756. https://doi.org/10.1002/2017jc013712

Kim, H.-S., Flagg, C. N., & Howden, S. D. (2001). Northern Arabian Sea variability from TOPEX/Poseidon altimetry data: An extension of the US JGOFS/ONR shipboard ADCP study. *Deep Sea Research Part II: Topical Studies in Oceanography*, *48*(6–7), 1069–1096. https://doi.org/10.1016/s0967-0645(00)00131-4

Kumar, S. P., & Prasad, T. G. (1999). Formation and spreading of Arabian Sea high-salinity water mass. *Journal of Geophysical Research*, *104*(C1), 1455–1464. https://doi.org/10.1029/1998jc900022

Le Vu, B., Stegner, A., & Arsouze, T. (2018). Angular Momentum Eddy Detection and Tracking Algorithm (AMEDA) and its application to coastal eddy formation. *Journal of Atmospheric and Oceanic Technology*, *35*(4), 739–762. https://doi.org/10.1175/jtech-d-17-0010.1

L'Hégaret, P., Beal, L. M., Elipot, S., & Laurindo, L. (2018). Shallow cross-equatorial gyres of the Indian Ocean driven by seasonally reversing monsoon winds. *Journal of Geophysical Research: Oceans*, *123*(12), 8902–8920.

L'Hégaret, P., Carton, X., Louazel, S., & Boutin, G. (2016). Mesoscale eddies and submesoscale structures of Persian Gulf water off the Omani coast in spring 2011. *Ocean Science*, *12*(3), 687–701.

L'Hégaret, P., Duarte, R., Carton, X., Vic, C., Ciani, D., Baraille, R., & Corréard, S. (2015). Mesoscale variability in the Arabian Sea from HYCOM model results and observations: Impact on the Persian Gulf water path. *Ocean Science*, *11*(5), 667–693.

Li, Y., & Wang, F. (2015). Thermocline spiciness variations in the tropical Indian Ocean observed during 2003-2014. *Deep Sea Research Part I: Oceanographic Research Papers*, *97*, 52–66. https://doi.org/10.1016/j.dsr.2014.12.004

Loaec, G., Cortes, N., Menzel, M., & Moliera, J. (1998). PROVOR: A hydrographic profiler based on MARVOR technology. In Paper presented at IEEE Oceanic Engineering Society. Oceans'98. Conference Proceedings (cat. no. 98ch36259) (Vol. 1, pp. 42–45).

Lueck, R. G., & Picklo, J. J. (1990). Thermal inertia of conductivity cells: Observations with a sea-bird cell. *Journal of Atmospheric and Oceanic Technology*, *7*(5), 756–768. https://doi.org/10.1175/1520-0426(1990)007<0756:tiocco>2.0.co;2

McDougall, T. J., & Barker, P. M. (2011). Getting started with TEOS-10 and the Gibbs seawater (GSW) Oceanographic Toolbox. *SCOR/IAPSO WG*, *127*, 1–28.

McDougall, T. J., & Krzysik, O. A. (2015). Spiciness. *Journal of Marine Research*, *73*(5), 141–152. https://doi.org/10.1357/002224015816665589

Mensah, V., Le Menn, M., & Morel, Y. (2009). Thermal mass correction for the evaluation of salinity. *Journal of Atmospheric and Oceanic Technology*, *26*(3), 665–672. https://doi.org/10.1175/2008jtecho612.1

Meunier, T., Ménesguen, C., Schopp, R., & Le Gentil, S. (2015). Tracer stirring around a meddy: The formation of layering. *Journal of Physical Oceanography*, *45*(2), 407–423. https://doi.org/10.1175/jpo-d-14-0061.1

Morrison, J. M., Codispoti, L., Gaurin, S., Jones, B., Manghnani, V., & Zheng, Z. (1998). Seasonal variation of hydrographic and nutrient fields during the US JGOFS Arabian Sea process study. *Deep Sea Research Part II: Topical Studies in Oceanography*, *45*(10–11), 2053–2101. https://doi.org/10.1016/s0967-0645(98)00063-0

Morvan, M., L'Hégaret, P., Carton, X., Gula, J., Vic, C., de Marez, C., & Koshel, K. (2019). The life cycle of submesoscale eddies generated by topographic interactions. *Ocean Science*, *15*(6). https://doi.org/10.5194/os-15-1531-2019

Morvan, M., L'Hégaret, P., de Marez, C., Carton, X., Corréard, S., & Baraille, R. (2020). Life cycle of mesoscale eddies in the Gulf of Aden. *Geophysical & Astrophysical Fluid Dynamics*, *114*(4–5), 631–649. https://doi.org/10.1080/03091929.2019.1708348

Ollitrault, M., Loaec, G., & Dumortier, C. (1994). MARVOR: A multi-cycle RAFOS float. *Sea Technology*, *35*(2), 39–44.

Owens, W. B., & Wong, A. P. S. (2009). An improved calibration method for the drift of the conductivity sensor on autonomous CTD profiling floats by θ-S climatology. *Deep Sea Research Part I: Oceanographic Research Papers*, *56*(3), 450–457. https://doi.org/10.1016/j.dsr.2008.09.008

Pegliasco, C., Chaigneau, A., & Morrow, R. (2015). Main eddy vertical structures observed in the four major eastern boundary upwelling systems. *Journal of Geophysical Research: Oceans*, *120*(9), 6008–6033. https://doi.org/10.1002/2015jc010950

Pous, S., Lazure, P., & Carton, X. (2015). A model of the general circulation in the Persian Gulf and in the strait of Hormuz: Intraseasonal to interannual variability. *Continental Shelf Research*, *94*, 55–70. https://doi.org/10.1016/j.csr.2014.12.008

Prasad, T. G., Ikeda, M., & Kumar, S. P. (2001). Seasonal spreading of the Persian Gulf water mass in the Arabian Sea. *Journal of Geophysical Research*, *106*(C8), 17059–17071. https://doi.org/10.1029/2000jc000480

Queste, B. Y., Vic, C., Heywood, K. J., & Piontkovski, S. A. (2018). Physical controls on oxygen distribution and denitrification potential in the North West Arabian Sea. *Geophysical Research Letters*, *45*(9), 4143–4152. https://doi.org/10.1029/2017gl076666

Quraishee, G. (1984). Circulation in the North Arabian Sea at Murray ridge during SW monsoon. *Deep Sea Research Part A. Oceanographic Research Papers*, *31*(6–8), 651–664. https://doi.org/10.1016/0198-0149(84)90033-5

Resplandy, L., Lévy, M., Madec, G., Pous, S., Aumont, O., & Kumar, D. (2011). Contribution of mesoscale processes to nutrient budgets in the Arabian Sea. *Journal of Geophysical Research: Oceans*, *116*(C11). https://doi.org/10.1029/2011jc007006

Roquet, F., Madec, G., McDougall, T. J., & Barker, P. M. (2015). Accurate polynomial expressions for the density and specific volume of seawater using the TEOS-10 standard. *Ocean Modelling*, *90*, 29–43. https://doi.org/10.1016/j.ocemod.2015.04.002

Rossby, T., Dorson, D., & Fontaine, J. (1986). The RAFOS system. *Journal of Geophysical Research*, *3*(4), 672–679. https://doi.org/10.1175/1520-0426(1986)003<0672:trs>2.0.co;2

Ruddick, B. (1983). A practical indicator of the stability of the water column to double-diffusive activity. *Deep Sea Research A. Oceanographic Research Papers*, *30*(10), 1105–1107. https://doi.org/10.1016/0198-0149(83)90063-8

Schmidt, H., Czeschel, R., & Visbeck, M. (2019). Ventilation dynamics of the oxygen minimum zone in the Arabian Sea. *Biogeosciences Discussions*, 1–32. https://doi.org/10.5194/bg-2019-168

Schott, F. A., & Fischer, J. (2000). Winter monsoon circulation of the northern Arabian Sea and Somali current. *Journal of Geophysical Research*, *105*(C3), 6359–6376. https://doi.org/10.1029/1999jc900312

Senjyu, T., Ishimaru, T., Matsuyama, M., & Koike, Y. (1998). High salinity lens from the strait of Hormuz. In *Offshore environment of the ROPME Sea area after the war-related oil spill* (pp. 35–48).

Shankar, D., Shenoi, S. S. C., Nayak, R. K., Vinayachandran, P. N., Nampoothiri, G., Almeida, A. M., et al. (2005). Hydrography of the Eastern Arabian Sea during summer monsoon 2002. *Journal of Earth System Science*, *114*(5), 459–474. https://doi.org/10.1007/bf02702023

Shapiro, G. I., & Meschanov, S. L. (1991). Distribution and spreading of Red Sea Water and salt lens formation in the northwest Indian Ocean. *Deep Sea Research Part A. Oceanographic Research Papers*, *38*(1), 21–34. https://doi.org/10.1016/0198-0149(91)90052-h

Sheehan, P. M., Webber, B. G., Sanchez-Franks, A., Matthews, A. J., Heywood, K. J., & Vinayachandran, P. (2020). Injection of oxygenated Persian Gulf water into the Southern Bay of Bengal. *Geophysical Research Letters*, *47*(14), e2020GL087773.

Shenoi, S. S. C., Shankar, D., Michael, G. S., Kurian, J., Varma, K. K., Kumar, M. R. R., et al. (2005). Hydrography and water masses in the southeastern Arabian Sea during March-June 2003. *Journal of Earth System Science*, *114*(5), 475–491. https://doi.org/10.1007/bf02702024

Shetye, S. R., Gouveia, A., & Shenoi, S. (1994). Circulation and water masses of the Arabian Sea. *Proceedings of the Indian Academy of Sciences - Earth & Planetary Sciences*, *103*(2), 107–123.

Shetye, S. R., Gouveia, A. D., Shenoi, S. S. C., Michael, G. S., Sundar, D., Almeida, A. M., & Santanam, K. (1991). The coastal current off western India during the northeast monsoon. *Deep Sea Research Part A. Oceanographic Research Papers*, *38*(12), 1517–1529. https://doi.org/10.1016/0198-0149(91)90087-v

Smith, K. S., & Ferrari, R. (2009). The production and dissipation of compensated thermohaline variance by mesoscale stirring. *Journal of Physical Oceanography*, *39*(10), 2477–2501. https://doi.org/10.1175/2009jpo4103.1

Tailleux, R., Lazar, A., & Reason, C. J. C. (2005). Physics and dynamics of density-compensated temperature and salinity anomalies. Part I: Theory. *Journal of Physical Oceanography*, *35*(5), 849–864. https://doi.org/10.1175/jpo2706.1

Todd, R. E., Rudnick, D. L., Mazloff, M. R., Cornuelle, B. D., & Davis, R. E. (2012). Thermohaline structure in the California current system: Observations and modeling of spice variance. *Journal of Geophysical Research*, *117*(C2). https://doi.org/10.1029/2011jc007589

Trott, C. B., Subrahmanyam, B., Chaigneau, A., & Delcroix, T. (2018). Eddy tracking in the Northwestern Indian ocean during southwest monsoon regimes. *Geophysical Research Letters*, *45*(13), 6594–6603. https://doi.org/10.1029/2018gl078381

Turner, J. S. (1979). *Buoyancy effects in fluids*. Cambridge University Press.

Vic, C., Roullet, G., Capet, X., Carton, X., Molemaker, M. J., & Gula, J. (2015). Eddy-topography interactions and the fate of the Persian Gulf Outflow. *Journal of Geophysical Research: Oceans*, *120*(10), 6700–6717. https://doi.org/10.1002/2015jc011033

Whalen, C., Talley, L., & MacKinnon, J. (2012). Spatial and temporal variability of global ocean mixing inferred from Argo profiles. *Geophysical Research Letters*, *39*(18). https://doi.org/10.1029/2012gl053196

Wong, A. P. S., Johnson, G. C., & Owens, W. B. (2003). Delayed-mode calibration of autonomous CTD profiling float salinity data by θ-S climatology. *Journal of Atmospheric and Oceanic Technology*, *20*(2), 308–318. https://doi.org/10.1175/1520-0426(2003)020<0308:dmcoac>2.0.co;2

Wyrtki, K. (1971). *Oceanographic atlas of the international Indian Ocean Expedition*. National Science Foundation.

Yao, F., & Johns, W. E. (2010). A HYCOM modeling study of the Persian Gulf: 2. Formation and export of Persian Gulf water. *Journal of Geophysical Research: Oceans*, *115*(C11). https://doi.org/10.1029/2009jc005788

Yeager, S. G., & Large, W. G. (2004). Late-winter generation of spiciness on subducted isopycnals. *Journal of Physical Oceanography*, *34*(7), 1528–1547. https://doi.org/10.1175/1520-0485(2004)034<1528:lgosos>2.0.co;2

You, Y. (2002). A global ocean climatological atlas of the turner angle: Implications for double-diffusion and water-mass structure. *Deep Sea Research Part I: Oceanographic Research Papers*, *49*(11), 2075–2093. https://doi.org/10.1016/s0967-0637(02)00099-7